NAVAL POSTGRADUATE SCHOOL

MONTEREY, CALIFORNIA

THESIS

EXPERIMENTAL ANALYSIS AND MODELING OF OPTICAL TURBULENCE IN THE MARITIME ENVIRONMENT AND ITS POTENTIAL EFFECT ON LASER COMMUNICATIONS

by

Georgios Chaskakis

December 2020

Thesis Advisor: Keith R. Cohn
Co-Advisor: Joseph A. Blau

THIS PAGE INTENTIONALLY LEFT BLANK

REPORT DOCUMENTATION PAGE	*Form Approved OMB No. 0704-0188*

1. AGENCY USE ONLY *(Leave blank)*	**2. REPORT DATE** December 2020	**3. REPORT TYPE AND DATES COVERED** Master's thesis

4. TITLE AND SUBTITLE
EXPERIMENTAL ANALYSIS AND MODELING OF OPTICAL TURBULENCE IN THE MARITIME ENVIRONMENT AND ITS POTENTIAL EFFECT ON LASER COMMUNICATIONS.

5. FUNDING NUMBERS

6. AUTHOR(S) Georgios Chaskakis

7. PERFORMING ORGANIZATION NAME(S) AND ADDRESS(ES)
Naval Postgraduate School
Monterey, CA 93943-5000

8. PERFORMING ORGANIZATION REPORT NUMBER

9. SPONSORING / MONITORING AGENCY NAME(S) AND ADDRESS(ES)
N/A

10. SPONSORING / MONITORING AGENCY REPORT NUMBER

11. SUPPLEMENTARY NOTES The views expressed in this thesis are those of the author and do not reflect the official policy or position of the Department of Defense or the U.S. Government.

12a. DISTRIBUTION / AVAILABILITY STATEMENT
Approved for public release. Distribution is unlimited.

12b. DISTRIBUTION CODE
A

13. ABSTRACT (maximum 200 words)

Free space optical (FSO) communication technology is increasingly used for both commercial and military purposes. For military communication that requires fast, secure, and reliable transmission of information, the benefits of using FSO technology are important. However, there are some inherent limitations, especially due to environmental conditions such as turbulence, that can significantly affect the performance of FSO communication systems.

Since turbulence plays a critical role in FSO systems, the purpose of this thesis is to compare different experimental and theoretical methods for estimating turbulence in a maritime environment. This analysis is achieved by measuring meteorological parameters using a local weather station and then using that data to calculate (using machine learning regression analysis) the refraction structure parameter that indicates the severity of turbulence. Also, the impact of turbulence on the signal-to-noise ratio (SNR) for a notional FSO system is estimated to show that even moderate amounts of turbulence can significantly reduce the SNR.

14. SUBJECT TERMS atmospheric turbulence, optical communications, free space optical, FSO, measurements, maritime environment, signal-to-noise ratio, SNR	**15. NUMBER OF PAGES** 99
	16. PRICE CODE

17. SECURITY CLASSIFICATION OF REPORT	**18. SECURITY CLASSIFICATION OF THIS PAGE**	**19. SECURITY CLASSIFICATION OF ABSTRACT**	**20. LIMITATION OF ABSTRACT**
Unclassified	Unclassified	Unclassified	UU

NSN 7540-01-280-5500

Standard Form 298 (Rev. 2-89)
Prescribed by ANSI Std. 239-18

THIS PAGE INTENTIONALLY LEFT BLANK

Approved for public release. Distribution is unlimited.

EXPERIMENTAL ANALYSIS AND MODELING OF OPTICAL TURBULENCE IN THE MARITIME ENVIRONMENT AND ITS POTENTIAL EFFECT ON LASER COMMUNICATIONS.

Georgios Chaskakis
Lieutenant Commander, Hellenic Navy
BNS, Hellenic Naval Academy, 2005

Submitted in partial fulfillment of the
requirements for the degree of

MASTER OF SCIENCE IN APPLIED PHYSICS

from the

NAVAL POSTGRADUATE SCHOOL
December 2020

Approved by: Keith R. Cohn
Advisor

Joseph A. Blau
Co-Advisor

Kevin B. Smith
Chair, Department of Physics

THIS PAGE INTENTIONALLY LEFT BLANK

ABSTRACT

Free space optical (FSO) communication technology is increasingly used for both commercial and military purposes. For military communication that requires fast, secure, and reliable transmission of information, the benefits of using FSO technology are important. However, there are some inherent limitations, especially due to environmental conditions such as turbulence, that can significantly affect the performance of FSO communication systems.

Since turbulence plays a critical role in FSO systems, the purpose of this thesis is to compare different experimental and theoretical methods for estimating turbulence in a maritime environment. This analysis is achieved by measuring meteorological parameters using a local weather station and then using that data to calculate (using machine learning regression analysis) the refraction structure parameter that indicates the severity of turbulence. Also, the impact of turbulence on the signal-to-noise ratio (SNR) for a notional FSO system is estimated to show that even moderate amounts of turbulence can significantly reduce the SNR.

THIS PAGE INTENTIONALLY LEFT BLANK

TABLE OF CONTENTS

LIST OF FIGURES

LIST OF TABLES

THIS PAGE INTENTIONALLY LEFT BLANK

LIST OF ACRONYMS AND ABBREVIATIONS

ASTD	air-sea temperature difference
AC	alternating current
CG	Coast Guard
EM	electromagnetic
3-D	three-dimensional
FSO	free space optics
FWTC	fine-wire thermocouple
H-V	Hufnagel Valley
IR	infrared
NOAA	National Oceanic and Atmospheric Administration
NAVSLAM	Navy Atmospheric Vertical Surface Layer Model
NPS	Naval Postgraduate School
PDF	probability density function
RMSE	root mean square error
SNR	signal-to-noise ratio
UV	ultraviolet
WP	waypoint
WWI	World War I

THIS PAGE INTENTIONALLY LEFT BLANK

ACKNOWLEDGMENTS

First of all, I would like to express my gratitude to the Hellenic Navy for giving me the opportunity to study at the Naval Postgraduate School.

Also, I would like to thank my advisors, Professors Keith Cohn and Joseph Blau, for their continuous support and guidance throughout my thesis research.

All my love to my wife, Kyriaki, and my two kids, Fotis and Thodoris, for inspiring and motivating me to complete this challenging journey successfully.

THIS PAGE INTENTIONALLY LEFT BLANK

I. INTRODUCTION

A. PROBLEM STATEMENT

Free space optical (FSO) communication technology is increasingly used for both commercial and military purposes. For military communication that requires fast, secure and reliable transmission of information, the benefits of using FSO technology are important. However, there are some inherent limitations, especially due to environmental conditions, that can significantly affect the performance of FSO communication systems. Therefore, an in-depth analysis of their performance, including environmental effects such as atmospheric turbulence, is considered critical for the understanding of the operation and use of these systems.

B. THESIS PURPOSE

Since turbulence plays a critical role in FSO systems, the purpose of this thesis is to compare different experimental and theoretical methods for estimating turbulence in a maritime environment. This analysis is achieved by measuring meteorological parameters using a local weather station, and then using that data to calculate (using machine learning regression analysis) the refraction structure parameter C_n^2 that indicates the severity of turbulence. Also, the impact of turbulence on the signal-to-noise ratio for a notional FSO system will be estimated.

C. THESIS ORGANIZATION

This thesis begins in Chapter I by indicating the overall goal of the study.

Chapter II describes the evolution of FSO communication systems, the advantages of using lasers in these systems, as well as the limitations of their use due to environmental conditions.

In Chapter III, a detailed analysis of atmospheric extinction and atmospheric turbulence phenomena and their effects on laser propagation is provided.

In Chapter IV, the experimentation is described.

Chapter V presents the experimental results, followed by some analysis and conclusions.

Lastly, conclusions and future work recommendations are provided at Chapter VI.

II. BACKGROUND

A. FREE SPACE OPTICAL / LASER COMMUNICATION TECHNOLOGY

Free space optical communication is a technology that uses light propagating through the atmosphere or outer space (i.e., instead of a fiber optic cable or radio frequency transmission) to transmit data. An FSO link must be line-of-sight (LOS) and also requires precise alignment between the source and the receiver [1].

FSO communication is not a new technology. The earliest FSO system are considered to have been invented by the ancient Greeks who used a coded system with flares to communicate over large distances [1]. Several centuries later, Graham Bell invented the photophone—a wireless device able to transmit sound using light—that deserves the title of the earliest FSO system of modern times [1], [2]. Also worth mentioning is the use of optical Morse code during World War I by German troops that made communication possible over distances of more than 5 kilometers [1], [2].

However, the more recent discovery of powerful, coherent optical sources (e.g., lasers in the 1960s), marked the beginning of a new era for FSO communication. Since that time, significant process has been made in the practical use of lasers for communication, especially following the rapid development of optoelectronics. Nowadays, research on laser communication technology is evolving with valuable applications in a variety of fields, including military and deep space applications [2].

B. ADVANTAGES

The key advantages that laser based FSO communication technology offers over radio frequency (RF) technology are the following:

1. High Bandwidth

Generally, laser communication systems are able to use a wide range of the electromagnetic (EM) spectrum, including infrared (IR), visible and ultraviolet (UV) sub-spectra. Thus, such systems operate at shorter wavelengths and therefore at higher frequencies compared to RF systems, achieving higher bandwidth capability than RF

systems with a much lower error rate [2]. However, at optical wavelengths, the interaction of EM radiation with the atmosphere is much stronger. Therefore, atmospheric phenomena such as atmospheric extinction and turbulence should be taken into account for the performance analysis of laser communication, as will be described in detail in the next chapter.

2. Narrow Beam Size

Lasers operate at much shorter wavelengths than RF sources; thus, a laser beam experiences much less spreading due to diffraction than a radio wave. Furthermore, laser light is coherent, so a laser beam can stay focused to a narrow size (i.e., beam radius on the order of cm or less) over large distances. This enables precise delivery of energy and information with less likelihood for detection or interference [2].

3. No License Restrictions

Laser communications do not require licensing (unlike RF communications). In RF communication technology, the spectrum is allocated to users to avoid interference between them; this is in contrast to laser communications, where optical frequencies are freely available for use and there is no need for licenses. That offers the advantage of quick installation and immediate use of laser communication systems, exempted from the time-consuming obligation of obtaining a license [2].

4. Less Susceptible to EM interference

Although EM interference affects RF communications to a high degree, it shows no effect on laser communication systems. EM interference, which is also known as radio frequency interference, could cause serious effects on RF communication channels by introducing noise and degrading them, something that cannot affect laser communications at all, as laser communication systems do not operate in the RF spectrum and, consequently, they are less susceptible to radio frequency interference [2].

5. Security

The transmitted energy of laser communication systems is concentrated in a very narrow beam and therefore the communication channel of such a system is very secure compared to a RF communication channel. This feature makes laser communication systems ideal, especially for military applications, as the narrow beam of these systems makes them very difficult to be intercepted [2].

C. LIMITATIONS

Despite the aforementioned advantages of laser communication systems, there are the following limitations that need to be considered:

1. Line-of-Sight (LOS) Communication

A significant limitation of a laser communication link is that it must be necessarily line-of-sight (LOS) because laser beams generally travel in a straight line (although they can bend slightly due to refractive layers in the atmosphere). This limitation results in communication not being possible for over the horizon or obscured terminal stations.

2. Atmospheric Effects

The performance of laser communications is strongly related to atmospheric conditions. There are two main atmospheric effects that may limit the performance of laser communications, as explained in the sections that follow.

a. Atmospheric Absorption and Scattering

Atmospheric absorption is caused by molecules and aerosols that can absorb photons along a laser beam's path. Another effect is atmospheric scattering, where molecules and aerosols absorb photons and then re-emit them in various directions. The combined effect of these phenomena is called extinction, which results in the irradiance of a laser beam decreasing, depending on the type and concentration of particles along the beam path [2]–[4].

b. Atmospheric Turbulence

A laser beam traveling in the atmosphere will pass through numerous regions with small, random fluctuations in the refractive index due to the varying temperature and density of the atmosphere. The random fluctuations of the refractive index can cause the laser beam to break apart and/or wander, depending on the beam parameters and the level of the fluctuations. This phenomenon, called optical turbulence, can cause an increase in the time-averaged spot size of the laser beam, thus decreasing the irradiance at the detector. More detrimental for communication applications is scintillation, which is fluctuations of the intensity at the detector due to turbulence. These fluctuations compete with the pulsed signal; the data transmission rate may need to be reduced to compensate for this effect [2]–[4].

3. Weather Effects

The efficiency of laser based FSO communication systems can be critically affected by the weather, including the following effects.

a. Haze/Fog/Rain

As mentioned in the paragraph above, the atmospheric molecules and aerosols are responsible for the phenomenon of atmospheric extinction. More specifically, fog/haze aerosols, whose diameters are comparable to the wavelength (~1.5 μm), can cause more laser radiation to scatter (per particle) relative to rain droplets (that are much larger in size at ~0.3 mm) [3]. The effect of atmospheric molecules and aerosols on laser propagation will be analyzed in more detail in the next chapter.

b. Temperature

Temperature variations can lead to optical turbulence along the laser beam path and thus affect optical communications. Temperature gradients from ground heating are one mechanism for the creation of turbulence, especially along optical paths close to the ground. As mentioned in the paragraph above, those atmospheric temperature variations can cause beam break-up or scintillation, resulting in a reduction of the irradiance at the terminal station.

D. SIGNAL-TO-NOISE RATIO IN AN FSO SYSTEM

Signal-to-Noise Ratio (SNR) is an important performance metric of an FSO system, with the following basic characteristics:

1. Source of Noise

The determination of the noise sources in an FSO system is a significant factor for estimating the system SNR. The photodiode in an FSO sensor in the receiver has two main noise sources:

a. Shot Noise

The shot noise results from the quantum nature of photons and electrons in the detector [15]. The fluctuations in photocurrent amplitude due to the shot noise in an optical system are given by

$$\sigma_{SN}{}^2 = 2eB\langle i_s \rangle, \tag{1}$$

where e =1.6× 10^{-19} C is the electric charge, B is the bandwidth of the detector (typical values range from 10^7 to 10^9 Hz), and $< i_s >$ is the average photocurrent in the detector circuit [15].

b. Johnson Noise

The Johnson noise arises from random thermal motion of the electrons in the detector circuit [15]. The Johnson noise in an optical system is proportional to the detector circuit temperatures and characterizes those temperature fluctuations as

$$\sigma_J{}^2 = \frac{4k_B T_B}{R}, \tag{2}$$

where $k_B = 1.38 \times 10^{-23}$ J/K is the Boltzmann constant, T_B is the absolute temperature in K, B is the bandwidth and R the resistance of the detector circuit [15].

c. Total Noise

The total noise in the detector is the sum of the shot σ_{SN}^2 and Johnson σ_J^2 contributions.

$$\sigma_N^2 \approx \sigma_{SN}^2 + \sigma_J^2 \ \ [\text{Ampere}^2] \tag{3}$$

2. Signal Current, $< i_s >$

As described previously, the shot noise depends upon the signal current (or photocurrent) $< i_s >$ generated in the detector circuit. In an FSO system, the $< i_s >$ is, roughly speaking, the signal current generated by the collected laser light by the detector. That signal current is given by

$$< i_s >= R_s P_{in}, \tag{4}$$

where R_s is the responsivity (in SI units of amps per watt) and P_{in} is the incident optical power on the detector [15]. The responsivity is a property of the photodiode in the detection system.

Figure 1 shows the propagation of a laser beam with an output power P_0 through an FSO system. The incident optical power P_{in} received on the detector is less than P_0, due to diffraction and atmospheric attenuation along the laser beam path. The optical power received by the detector depends on the beam radius w_L at the time that light reaches the detector and the diameter D of the detector [15]. The beam radius w_L depends on the angular spread θ and the propagation distance L and is equal to $w_L \sim \theta L$ [15]. The beam power decays exponentially due to scattering and absorption, resulting in the received power on the detector

$$P_{in} \approx P_0 e^{-\varepsilon L}, \quad \text{if} \quad w_L < D/2 \tag{5}$$

or

$$P_{in} \approx P_0 e^{-\varepsilon L} \left(\frac{D}{2w_L}\right)^2, \quad \text{if} \quad w_L > D/2, \tag{6}$$

according to Beer's law, which is described in more detail in the next chapter [15].

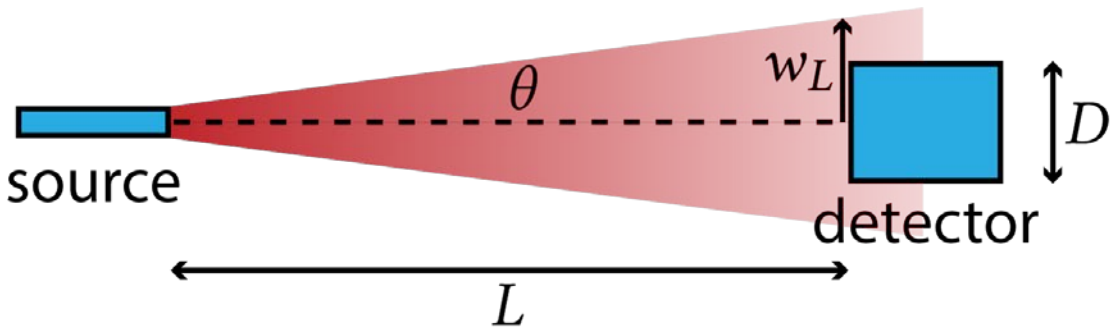

Figure 1. Laser light propagation through an FSO system

3. SNR of Detector (No turbulence)

The SNR of the detector, in an ideal condition (no turbulence) is given by

$$SNR_0 = \frac{<i_s>^2}{\sigma_N^2}. \quad (7)$$

The SNR_0 value should be much greater than 1 for the system to suffer no losses, i.e. $< i_s >^2 \gg \sigma_N^2$. This means that the generated photocurrent value is sufficient for the FSO system detector to be efficiently operated, despite the noise in the detector [15].

Atmospheric effects such as turbulence create additional effective contributions to the noise, reducing the signal-to-noise ratio. This process will be discussed in more detail in the next chapter.

THIS PAGE INTENTIONALLY LEFT BLANK

III. THEORY OF ATMOSPHERIC PROPAGATION

A. ATMOSPHERIC EXTINCTION

1. Beer's Law

During the propagation of laser radiation in the terrestrial atmosphere, molecules and aerosols that are suspended in the atmosphere absorb optical power along the laser beam's path. Additionally, the laser radiation interacts with the suspended particles and can be scattered in random directions. The combination of these two phenomena—absorption and scattering—is called atmospheric extinction [3]–[5].

Extinction over an arbitrary path through the atmosphere causes laser power to decay exponentially according to Beer's law

$$P(s_2) = P(s_1)e^{-\int_{s_1}^{s_2} \varepsilon(s)ds}, \tag{8}$$

where $P(s_1)$ the power of the incident radiation beam at position s_1, $P(s_2)$ is the power of the beam after propagating to position s_2, ε is the extinction coefficient, and ds is an infinitesimal displacement along the propagation path, as shown in Figure 2. The value of the extinction coefficient ε in Equation 8 can vary along the path and also depends on wavelength, location, time of the day, and other weather conditions [3]–[5].

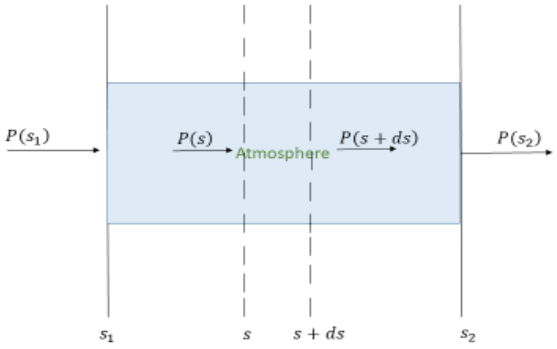

Figure 2. Decay of power due to extinction of a laser beam passing through the atmosphere. Adapted from [3].

Equation 8 can also be rearranged to express other figures of merit that are related to extinction, as

$$P(s_2) = P(s_1)e^{-\tau(s_1,s_2)} = P(s_1)t(s_1,s_2); \tag{9}$$

here, the definitions of optical depth $\tau(s_1,s_2)$ and transmittance $t(s_1,s_2)$ over an arbitrary path are introduced, where

$$\tau(s_1,s_2) \equiv \int_{s_1}^{s_2} \varepsilon(s)ds \tag{10}$$

and

$$t(s_1,s_2) \equiv \frac{P(s_2)}{P(s_1)} \equiv e^{-\int_{s_1}^{s_2}\varepsilon(s)ds} \equiv e^{-\tau(s_1,s_2)}. \tag{11}$$

Equations 10 and 11 denote that both optical depth and transmittance are dimensionless and positive. Transmittance indicates the total fraction of radiation $P(s_2)/P(s_1)$ that propagates through the medium and, therefore, varies from 0 (completely

opaque) to 1 (completely transparent). Optical depth is indicative of the transparency and/or opacity level of the atmosphere and can take any positive value; the larger the value, the greater the extinction. As Figure 3 shows, when $\tau(s_1, s_2) << 1$ the value of $t(s_1, s_2)$ approaches 1 and the extinction medium is considered as transparent or optically 'thin'; when $\tau(s_1, s_2) >> 1$, the extinction medium becomes more opaque or optically 'thick' and, therefore, there is increased probability of a photon's interaction with atmospheric particles [3,5], and the transmittance approaches zero.

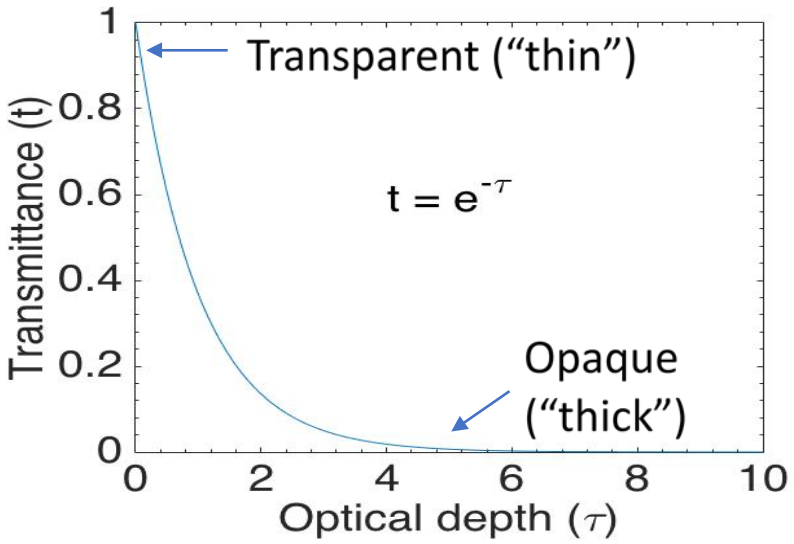

Figure 3. Optical depth τ over transmittance t. Source: [3].

The extinction coefficient, ε, is the sum of both absorption and scattering contributions

$$\varepsilon = \alpha_m + \alpha_a + \beta_m + \beta_a, \tag{12}$$

where the *m* and *a* subscripts indicate molecular and aerosol contributions to both absorption (α) and scattering (β), respectively. The total extinction is determined by the value of each of the four coefficients of Equation 12 at each point along the beam path [3].

Figure 4 displays the variation of the overall extinction coefficient as a function of wavelength for a typical summer, mid-latitude, maritime environment (MODTRAN simulation).

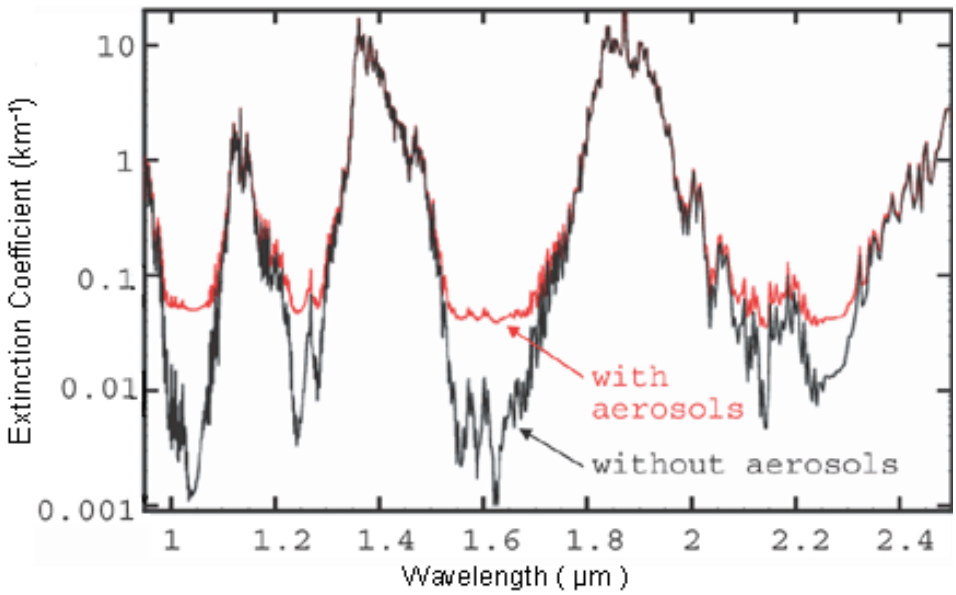

Figure 4. Variation of the extinction coefficient ε for different wavelengths, for typical summer, mid-latitude, maritime environment (MODTRAN simulation) Source: [3].

It is interesting to note from Figure 4 how the extinction coefficient varies by orders of magnitude with wavelength (note the log scale on the vertical axis). Observing the horizontal axis of this figure, it is obvious only certain wavelengths in the 1 μm to 2.5 μm window are acceptably transparent: around 1 μm, 1.6 μm and 2.2 μm. Moreover, the plot also shows large peaks in the extinction coefficient around 1.2 μm, 1.4 μm, and 2 μm, which indicates greater atmospheric opacity for these wavelengths.

2. Molecular Absorption: α_m

Molecules absorb at photon energies that correspond to quantum transitions between discrete energy levels. In the IR spectrum, most of these transitions correspond to vibrational or rotational transitions. Additionally, a change in the dipole moment as the molecule vibrates is needed to couple strongly to the electromagnetic field in order for

strong absorption to occur. This is primarily satisfied by several atmosphere components, as shown in Figure 5, which displays the total percentage of sunlight attenuated by the atmosphere (top plot) and the major components to that attenuation (lower plots) [3].

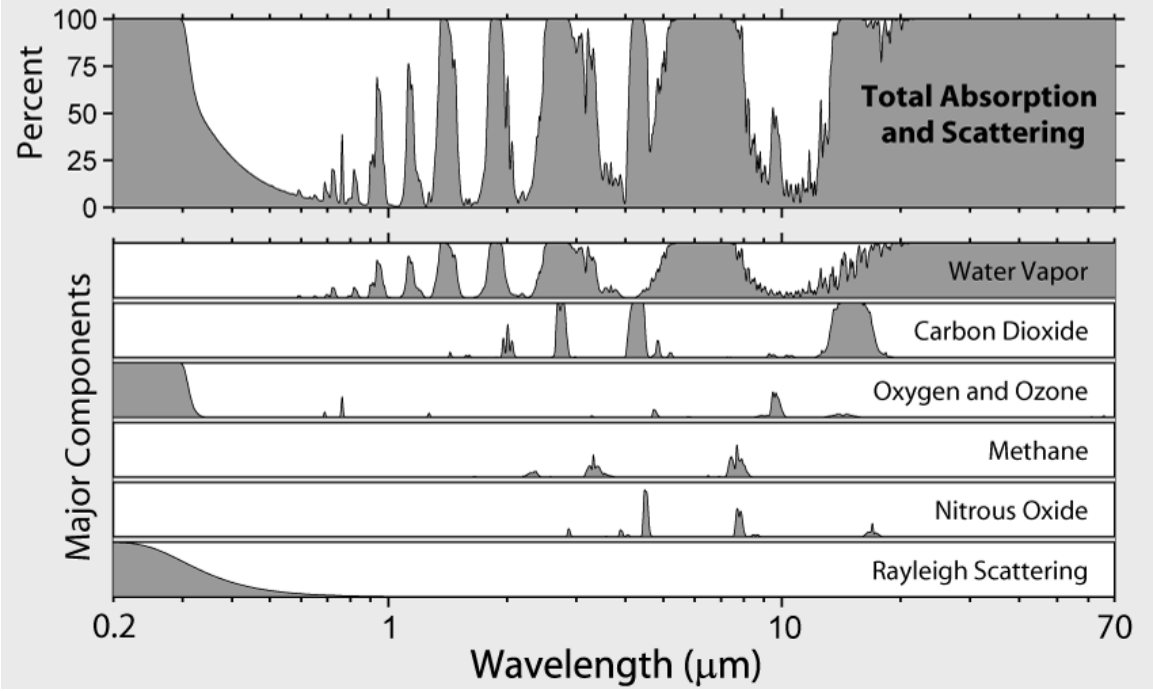

Figure 5. Typical total absorption and scattering spectrum and the contributions due to the major atmosphere components. Source: [3].

It is obvious from the figure that water vapor is the strongest contributor to atmospheric attenuation in the IR spectrum—this is especially a concern in a maritime environment. Oxygen and nitrogen show almost no absorption of radiation in the IR spectrum since they are diatomic molecules with dipole moments that do not change as these molecules vibrate.

3. Mie Scattering Theory: α_a, β_a, β_m

Mie scattering theory describes the phenomenon of light scattering from spherical particles. The theory can be used to describe the molecular and aerosol scattering

coefficients β_m and $\beta_{\alpha,}$ respectively, as well as the aerosol absorption coefficient α_α. Mie theory is based on the following assumptions:

- The atmospheric scattering is caused by homogeneous and spherically shaped particles [5].
- The scattered field is evaluated at a very large distance from the spherically shaped particles [5].
- The medium of propagation is homogeneous and isotropic [5].
- The atmospheric scattering is caused by a single particle that is isolated from the others. In this case, the atmospheric particles are assumed to not interact with each other, and the total atmospheric scattering is assumed to be the sum of each individual particle's contribution to the phenomenon [5].

Although the above-mentioned assumptions are not, strictly speaking, true, they are incorporated to facilitate the theory's mathematical approach to the phenomenon of atmospheric scattering.

Taking into consideration the assumptions of Mie scattering theory, the radiation intensity that is scattered by an atmospheric particle, is

$$I(\theta) = I_0\left(\frac{\sigma_s}{r^2}\right)\frac{P(\theta)}{4\pi}, \tag{13}$$

where I_0 is the incident intensity, r is the distance between the particle and observer , σ_s is the scattering cross section, θ is the scattering angle with respect to the incident beam, and $P(\theta)$ is the normalized phase function [5].

Equation 13 shows that the scattered radiation intensity I is proportional to the scattering cross section σ_s . Furthermore, Mie theory predicts the scattering cross section assumes the form

$$\frac{\sigma_s}{\pi\rho^2} = c_1 x^4 \left(1 + c_2 x^2 + c_3 x^4 + ...\right), \tag{14}$$

where

$$x \equiv \frac{2\pi\rho}{\lambda}, \tag{15}$$

ρ is the particle's radius, and λ is the wavelength [5]. Therefore, x is a dimensionless quantity that relates a particle's size to the wavelength. The c coefficients incorporate optical properties of the scattering object and can be estimated from Mie theory.

The total extinction cross section σ_e can also be derived from Mie theory, which is related to scattering and absorption by

$$\sigma_e = \sigma_\alpha + \sigma_s. \tag{16}$$

All of these cross sections are related to the extinction coefficients in Beer's law by integrating the cross sections with the number densities N over all particle radii; for example,

$$a_a(\lambda) = \int N(r)\sigma_\alpha(r)dr \tag{17}$$

and

$$\beta_a(\lambda) = \int N(r)\sigma_s(r)dr. \tag{18}$$

a. Rayleigh Scattering: β_m

Rayleigh scattering describes the phenomenon of atmospheric scattering by molecules. In this limit, the radius ρ is much smaller than the wavelength λ of the incident radiation, so $x \ll 1$. Therefore, only the lowest order term of Equation 14 contributes significantly to the molecular scattering cross section. This means that the molecular

scattering cross section (and corresponding scattering coefficient) is strongly wavelength dependent [3], [5]:

$$\beta_m \propto 1/\lambda^4 \tag{19}$$

as is shown schematically in the following Figure 6.

The wavelength dependence of Rayleigh scattering explains the color of the sky; specifically, the sky is blue during the day and red at sunset. In the visible spectrum, the blue color wavelength varies from 0.450 μm to 0.480 μm, while the red color wavelength varies from 0.625 μm to 0.740 μm. Since blue light is scattered more than all other colors of the visible spectrum, the daytime sky (on a clear day) is blue. At sunset, as the sun approaches the horizon, the sunlight passes through a thicker layer of atmosphere and, therefore, colors of shorter wavelengths are strongly scattered out of the sunlight, resulting in the sun appearing to be red [3], [5].

b. Aerosol Absorption and Scattering Coefficients α_a, β_a

The radius ρ of atmospheric aerosols such as smoke, dust, and smog, varies from approximately 0.1 μm to several microns and thus their size parameter x is of order 1. In this limit, the strong dependence of scattering on the wavelength that appeared in Rayleigh scattering drops out. Therefore, in the case of atmospheric aerosol scattering, the scattered radiation intensity is (roughly) independent of wavelength as shown in Figure 6. This explains why clouds appear white: the tiny water droplets in clouds scatter all optical wavelengths with approximately the same efficiency.

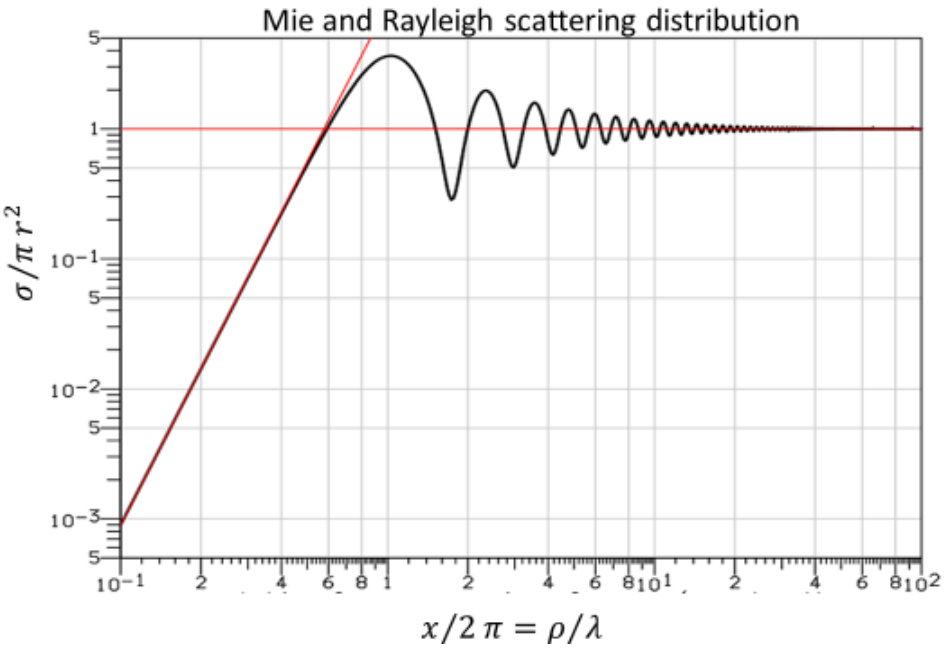

Figure 6. Mie and Rayleigh scattering distribution. Source: [6].

B. ATMOSPHERIC TURBULENCE

Optical turbulence is a phenomenon that occurs when optical rays traveling in the atmosphere experience random, small-scale fluctuations of temperature and density and thus refractive index. These random disturbances of the refractive index cause phase fluctuations of the wavefront, deflecting the optical rays and leading to break-up and wander of the optical beam. More critical from the perspective of FSO communications is an effect known as scintillation, which is the random intensity variations at the receiver due to the aforementioned effects [3], [7], [9].

1. Characterization of Turbulence

a. Refractive Index Structure Function D_n

The refractive index structure function D_n characterizes the refractive index fluctuations between two points—a point of interest and a nearby point—and is defined as

$$D_n(\Delta r) = < \left| n(\vec{r}) - n(\vec{r} + \Delta\vec{r}) \right|^2 >, \tag{20}$$

where n is the index of refraction, $\vec{r}$ the point of interest, and $\Delta\vec{r}$ the displacement vector from the point of interest to the nearby point, as shown in Figure 7. Equation 20 characterizes the refractive index variations over the surface of the sphere by averaging the square of the refractive index changes over a displacement of length $\overrightarrow{\Delta r}$, denoted by the brackets $<\left|.....\right|^2>$.

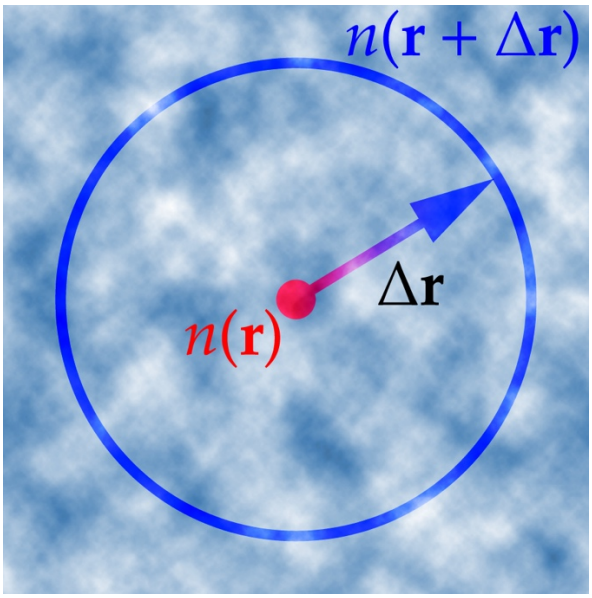

Figure 7. The refractive index fluctuations over a spherical surface of radius Δr. Source: [3].

The refractive index structure function D_n is the basis for theories that describe the statistics of atmospheric turbulence. Due to the stochastic nature of atmospheric turbulence, the development of such theories required the use of these statistical models to be able to estimate the effects of atmospheric turbulence on the propagation of optical beams. The most widely accepted theory is the Kolmogorov theory, as described analytically in the next section.

b. Kolmogorov Theory

The Kolmogorov theory of turbulence provides a simple analytical form for the structure function. The initial injection of energy for turbulence is driven by heat

conduction from the ground and wind shear. Kolmogorov reasoned that atmospheric turbulence is characterized by numerous air cells (or "eddies") of different sizes. According to Kolmogorov theory, an energy cascade happens from larger to smaller eddies, where the energy is injected at the largest eddy sizes, then is transferred successively to smaller ones, until finally the eddy motion is damped due to viscosity at the smallest sizes, as shown schematically in Figure 8. At that point, the energy of atmospheric turbulence is converted into heat.

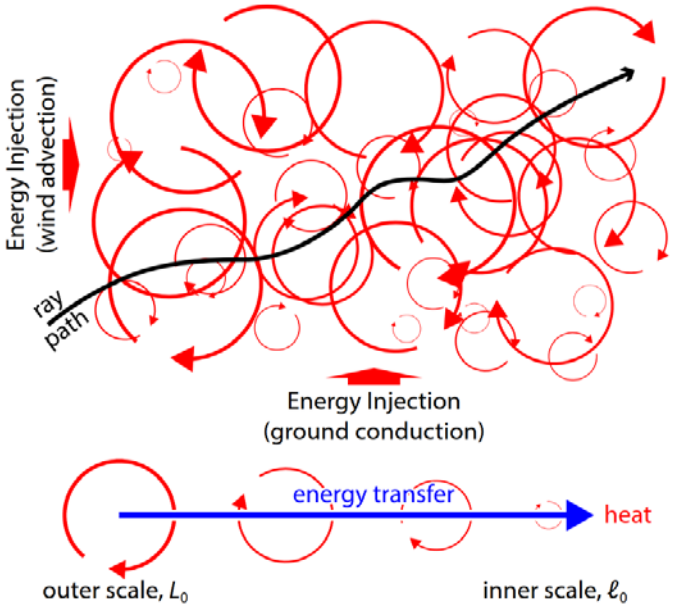

Figure 8. The cascade of energy as it transfers from the largest eddies to smaller ones, and eventually into thermal energy due to viscosity.
Source: [3].

More analytically, Kolmogorov theory predicts this relationship for the structure function

$$D_n(\Delta r) = C_n^2 (\Delta r)^{2/3}, \quad l_0 << \Delta r << L_0, \tag{21}$$

where L_0 and l_0 are the average sizes of the largest and smallest eddies, respectively, in the energy cascade [8]. Typical values for these length scales are on the order of meters for

L_0 and millimeters for l_0. Length scales within this range are often called the "inertial subrange." The coefficient C_n^2 is called the refractive index structure parameter, and a hallmark of Kolmogorov turbulence theory is that this coefficient is reasonably constant over length scales within the inertial subrange at a given point and time. This parameter quantifiably describes the severity of optical turbulence, where larger values correspond to larger fluctuations of the refractive index.

Figure 9 shows the results of simulations of the propagation of a laser beam over 1 km both with negligible and significant turbulence. Propagation through weak turbulence ($C_n^2 = 10^{-18}\ m^{-2/3}$) propagation is on the left, while propagation through moderately strong turbulence ($C_n^2 = 10^{-14} m^{-2/3}$) is on the right. In the left plot of Figure 9, where the laser is propagating in weak turbulence, the beam energy is well-focused, while on the right, the beam's energy is diffused due to turbulence.

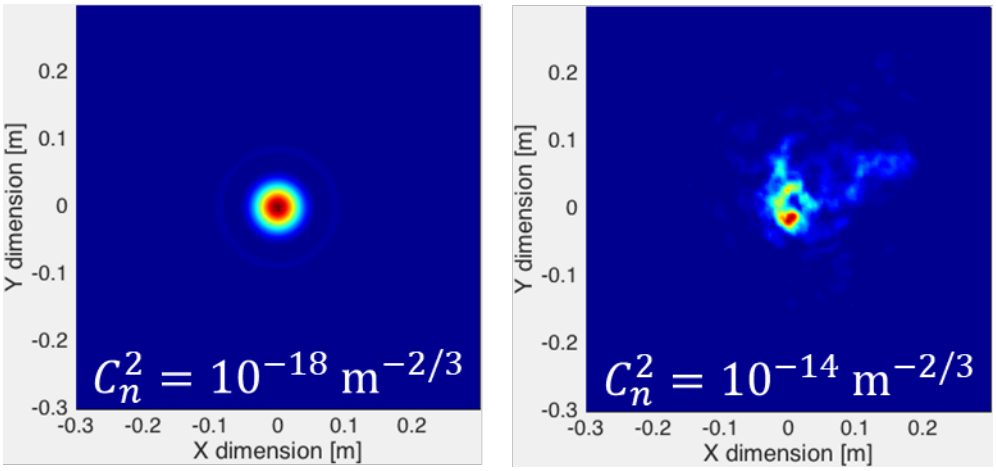

Figure 9. Simulation of a laser beam propagating over 1 km through weak turbulence (left) and through moderately strong turbulence (right). Source: [3].

2. C_n^2 Profiles

The refractive index structure parameter C_n^2 is an altitude-dependent parameter. Two characteristic models that indicate the altitude-dependency of C_n^2 are described in the paragraphs below.

a. Hufnagel Valley (H-V) Turbulence Model

The H-V Model describes how the refractive index structure parameter C_n^2 varies with altitude,

$$C_n^{\ 2}(h) = 8.2\times10^{-26}W^2h^{10}e^{-h} + 2.7\times10^{-16}e^{-h/1.5} + Ae^{-h/0.1}, \tag{22}$$

where h is the height in meters and W is the root mean squared wind speed over the 5 to 20 kilometers range [11]. This model is more valid near the Earth's surface where the convection from the ground has a significant effect on atmospheric temperature and therefore on the value of C_n^2.

The variation of C_n^2 with altitude according to the H-V Turbulence Model is shown in Figure 10. Analyzing this figure, it is obvious that C_n^2 tends to decrease significantly as the altitude increases up to about 5 km, and then starts to increase somewhat.

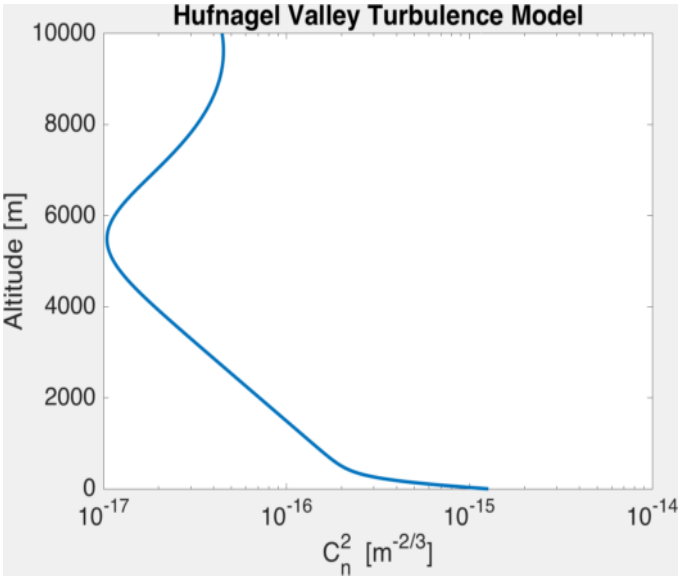

Figure 10. The altitude-dependent H-V Turbulence Model. Source: [3].

b. Navy Atmospheric Vertical Surface Layer Model

The Hufnagel-Valley model is, more or less, a static model that does not accurately describe turbulence in a maritime environment, especially near the surface. For example, C_n^2 is highly affected by the air-sea temperature difference (ASTD), but this is not accounted for in the Hufnagel-Valley model. Furthermore, the H-V model was developed based on observations at White Sands Missile Range, so it is more valid over land (in particular, the desert) than over the ocean.

The Navy Atmospheric Vertical Surface Layer Model (NAVSLaM), developed by the Department of Meteorology of Naval Postgraduate School (NPS), includes as inputs the wind speed, air and sea temperatures, humidity, and pressure, and then computes vertical turbulence C_n^2 within the surface layer (i.e., up to about 100 m) [3], [7]. This model is based on Monin-Obukhov similarity (MOS) theory and empirical functions extracted from at sea measurements and it is valid for wavelengths $0.3\mu m \leq \lambda \leq 14\mu m$ [3], [7].

Figure 11 plots the refractive index structure parameter C_n^2 profile versus height, depending on the ASTD, based on the NAVSLaM model. The profile of C_n^2 in unstable conditions, when the air is colder than sea (ASTD < 0), decreases more rapidly with height than it does in stable conditions, when air is warmer than sea (ASTD >0). Moreover, the value C_n^2 is much smaller for neutral conditions when ASTD ≈ 0 [7].

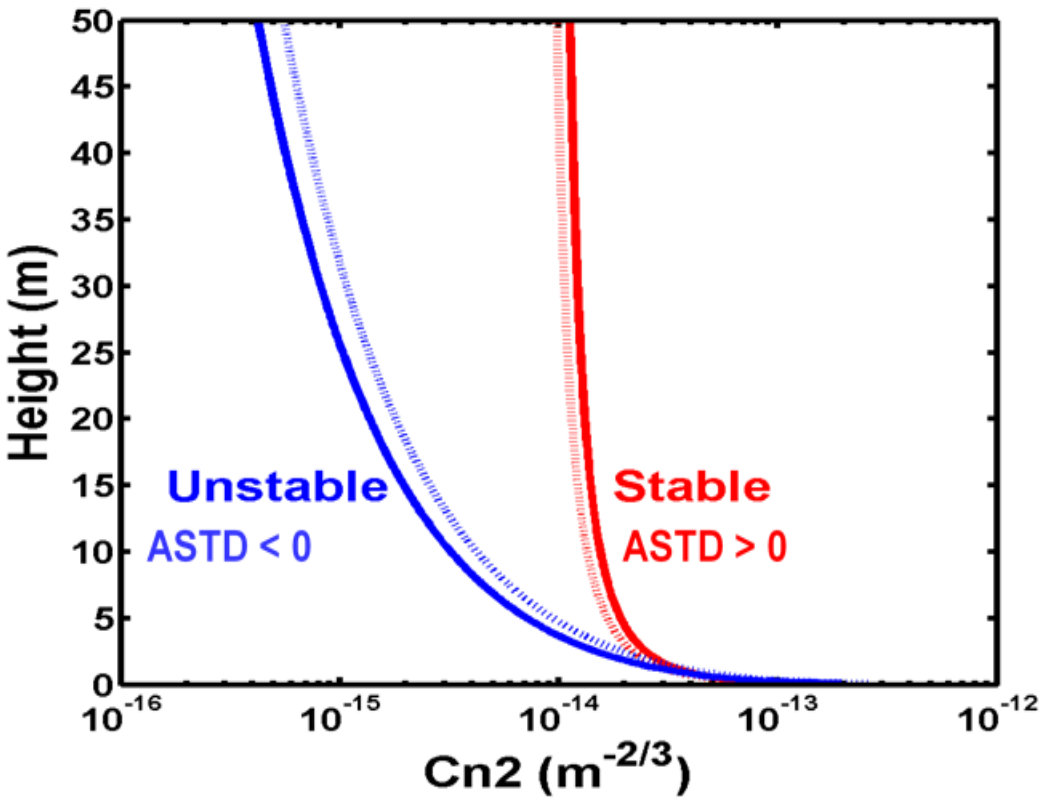

Figure 11. NAVSLaM Vertical C_n^2 profiles for different stabilities. Source: [3].

3. Fried Parameter r_0

The Fried parameter r_0 defines the diameter over which the laser beam maintains transverse coherence throughout the propagation length, taking into account the refractive index structure parameter C_n^2 along the path and the optical wavelength, and is defined for a spherical wave as

$$r_0 = \left[0.423(k)^2 \int_0^L C_n^2(z) \left(1 - \frac{z}{L}\right)^{5/3} dz \right]^{-3/5}, \tag{23}$$

where k is the wavenumber and L is the total length of the laser path [10].

The Fried parameter r_0 is an inversely proportional function of C_n^2, as is shown in Equation 23, and therefore strong turbulence is associated with small r_0, while weak

turbulence indicates large r_0. Also, r_0 can become small even in weak turbulence if the propagation distance L is long.

The scale in Figure 12 is called Pickering's scale, and it can demonstrate the impact that different r_0 values have on the beam. Analyzing Figure 12, it is evident that the smaller the Fried parameter in relation to the laser beam diameter *D*, the less cohesive the laser beam is. When the ratio $D \geq r_0$, turbulence significantly impacts the beam propagation and causes the beam to break up.

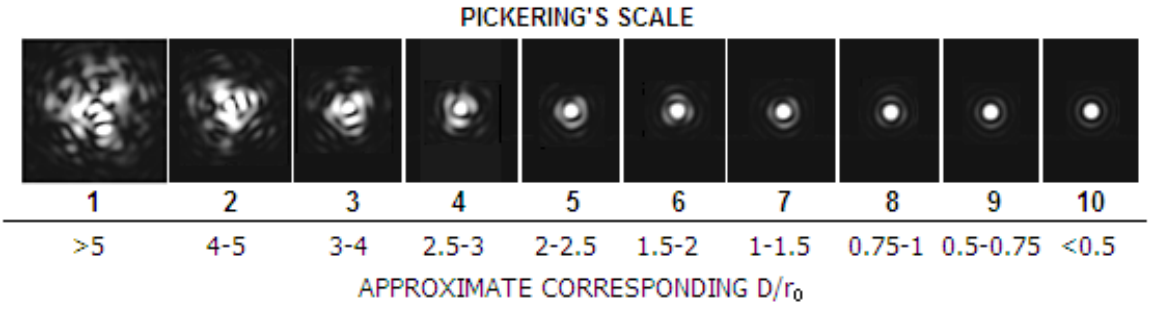

Figure 12. Pickering's scale. Source: [3].

C. IMPACT OF TURBULENCE ON FSO PERFORMANCE

There are multiple steps to estimate the influence that turbulence has on an FSO system, as described in the following sections.

1. Scintillation Index, σ_I^2

The optical turbulence is a serious issue for FSO systems since it can lead to optical signal intensity variations—called scintillation—at the detector. The twinkling of stars in the sky is a common example of the scintillation process. These intensity fluctuations are measured by the scintillation index σ_I^2, which indicates the severity of scintillation, and is defined by

$$\sigma_I^{\,2} = \frac{< I(r)^2 > - < I(r) >^2}{< I(r) >^2}, \tag{24}$$

where $I(r)$ is the intensity of the optical wave and the brackets <……> denote a time average [15]. The scintillation index σ_I^2 is dimensionless and the larger value of σ_I^2 means that more scintillation occurs.

2. Dependence of σ_I^2 on Turbulence

The turbulence tends to increase the scintillation index up to a saturation point. For a spherical wave, the scintillation index σ_I^2 is related to the refractive index structure parameter $\mathrm{C_n^2}$, which describes the severity of turbulence, by the following Equation:

$$\sigma_{\mathrm{I}}^2 \approx \exp\left[\frac{0.2\sigma_R^2}{\left(1+0.19\sigma_R^{12/5}\right)^{7/6}} + \frac{0.2\sigma_R^2}{\left(1+0.23\sigma_R^{12/5}\right)^{5/6}}\right] - 1, \tag{25}$$

where $\sigma_R^2 = 1.23\ \mathrm{C_n^2} k^{7/6} L^{11/6}$ is called the Rytov variance and actually contains the $\mathrm{C_n^2}$ dependence in Equation 25, k=2π/λ is the optical wavenumber and L the propagating distance [15]. The turbulence along the path is considered impactful when $\sigma_R^2 \gtrsim 0.3$ [15]. This can occur even in weak turbulence for long propagation distances.

3. Degradation of SNR from Turbulence

The effect of turbulence and, consequently, of scintillation on an optical signal traveling in the atmosphere is that it increases the effective noise of an FSO sensor; this reduces the signal-to-noise ratio (SNR) of its detector [15]. That effect can be somewhat mitigated by using a large aperture at the detector, since in that case more light intersects with the detector and therefore the effect of scintillation is reduced. That phenomenon is called aperture averaging [15].

In the case of a detector with a finite aperture radius, the scintillation index σ_I^2 can be estimated by

$$\sigma_{I,eff}^2(D) \approx \exp\left[\frac{0.49\beta_R^2}{\left(1+0.18d^2+0.56\beta_R^{12/5}\right)^{7/16}}+\frac{0.51\beta_R^2\left(1+0.69\beta_R^{12/5})^{-5/6}\right)}{1+0.9d^2+0.62d^2\beta_R^{12/5}}\right]-1, \qquad (26)$$

where $\beta_R^2 = 0.4\sigma_R^2$, d=$\sqrt{\frac{kD^2}{4L}}$, and D is the receiver aperture diameter.

It is noticed that as D becomes larger, the denominator of both terms in the brackets in Equation 26 is increased as well; this results in the reduction of the effective scintillation index $\sigma_{I,eff}^2$ [15]. Note that Equation 26 reduces to Equation 25 for a point detector (i.e., when $D = 0$).

An estimation of the effective SNR of an FSO communication system is given by

$$SNR = \frac{SNR_0}{\left[1+1.33\sigma_I^2\left(\frac{2L}{\kappa w_L^2}\right)^{5/6}\right]+F\sigma_I^2 SNR_0}, \qquad (27)$$

where F=$\frac{\sigma_{I,eff}^2}{\sigma_I^2}$, and SNR_0 is the SNR of a detector when there is no turbulence (from Equation 7) [15]. This is the equation that will be used to estimate the impact of experimentally measured turbulence on a notional FSO system in subsequent chapters of this thesis.

IV. EXPERIMENTAL CONFIGURATION

The experimental purpose of this thesis is to measure the turbulence across a maritime pathway. One of the reasons for doing this will be to develop a regression model of the refractive structure parameter C_n^2 from simple meteological data. The model is constructed by correlating local meteorological parameters—collected by a local weather station—and C_n^2 measurements taken by using the MZA DELTA. Another reason is to compare different methods of estimating C_n^2 from measurements.

A. EXPERIMENTAL EQUIPMENT

The equipment that was used for the thesis experiment is described in the following sections.

1. Ambient Weather WS-2000 OSPREY Solar-Powered Wireless Weather Station

The WS-2000 weather station includes an array of sensors in its base station that are able to measure the following meteorological elements:

- Temperature (Thermometer)
- Humidity (Hygrometer)
- Wind Speed (Anemometer)
- Wind Direction (Wind Vane)
- Rain Fall (Self-Emptying Rain Collector)
- Solar Radiation

The meteorological data, which are collected by the base station, can be displayed in a separate tablet style high definition and liquid crystal display console with dimensions of 6.25 x 3.5 inches. The display can be powered by a 5 V DC source [12].

The WS-2000 weather base station utilizes wireless technology to transmit to the display over a distance of up to 300 feet using a frequency of 915 MHz. Another great feature of the WS-2000 base station is that it uses solar energy as its primary power source. Additionally, it has a battery back-up system for days with little sunlight [12]. A picture of the WS-2000 weather station (base and display) is shown in the Figure 13.

Figure 13. The Ambient Weather WS-2000 OSPREY solar-powered wireless weather station. Source: [12].

Table 1 provides the specifications for the measured parameters according to the WS-2000 weather station user manual. It is also worth mentioning the fact that the WS-2000 weather station covers most environmental conditions and also show great resolution and accuracy of measurements.

Table 1. WS-2000 weather station measurement specifications.
Source: [12].

Measurement	Range	Accuracy	Resolution
Indoor Temperature	14 to 140°F	± 2°F	0.1 °F
Outdoor Temperature	-40 to 149°F (lithium batteries) -23 to 140°F (alkaline batteries)	± 2°F	0.1 °F
Indoor Humidity	10 to 99%	± 5%	1%
Outdoor Humidity	10 to 99%	± 5%	1%
Barometric Pressure	8.85 to 32.50 inHg	±0.08 inHg (within range of 27.13 to 32.50 inHg)	0.01 inHg
Light	0 to 200,000 Lux	± 15%	1 Lux
Rain	0 to 236 in.	± 5%	0.01 in
Wind Direction	0-360°	± 10°	1°
Wind Speed	0 to 100 mph (operational)	± 2.2 mph or 10% (whichever is greater)	1.4 mph

2. CSAT3 Three- Dimensional Sonic Anemometer

The principle of operation of the three-dimensional (3-D) sonic anemometer CSAT3 is based on measuring the wind speed and the speed of sound by determining the transit times of sound pulses traveling between pairs of opposing transducers [13]. In the case of a 3-D sonic anemometer, three pairs of transducers determine the 3-D wind vector, as shown schematically in Figure 14.

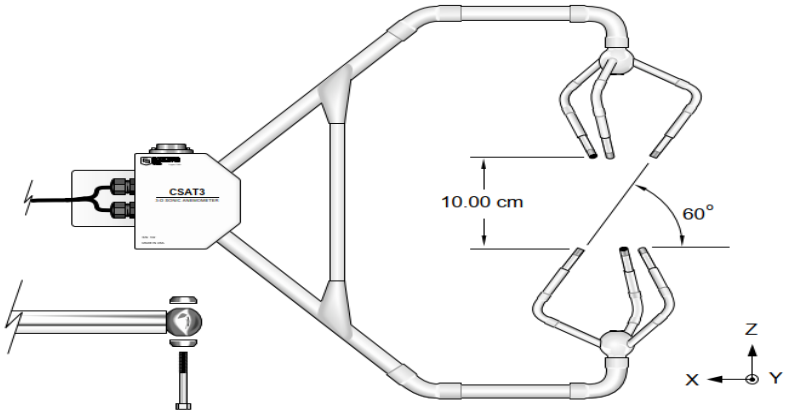

Figure 14. 3-D coordinate system of transducers of CSAT3 sonic anemometer. Source: [13].

Specifically, the times t_1 and t_2 during which the sonic pulses travel out and back along each pair of transducers are determined by

$$t_1^{x,y,z} = \frac{d}{c + u_{x,y,z}} \tag{28}$$

and

$$t_2^{x,y,z} = \frac{d}{c - u_{x,y,z}}, \tag{29}$$

where d is the distance between the transducers, c is the speed of sound, and u is the wind speed along any transducer axis [13].

The wind speed as well as the speed of sound can be found by the simultaneous solution of Equations 28 and 29, as

$$u_{x,y,z} = \frac{d}{2}\left[\frac{1}{t_1} - \frac{1}{t_2}\right] \tag{30}$$

$$c = \frac{d}{2}\left[\frac{1}{t_1} + \frac{1}{t_2}\right]. \tag{31}$$

Ultimately, we are interested in using the sonic anemometers to measure optical turbulence. The optical turbulence is due to refractive index variations of the air. As already discussed, according to Kolmogorov theory, atmospheric turbulence consists of numerous air cells (eddies) of different sizes and refractive indices, and whose dynamics are driven by energy from ground heat conduction and wind shear. This energy is injected at the largest eddy sizes. Then, an energy cascade occurs from larger to smaller eddies until the point that the kinetic energy dissipates as heat at the smallest eddy sizes due to viscosity.

The air refractive index variations are directly correlated to air temperature and density fluctuations. The sonic air temperature can be estimated from the measured speed of sound in Equation 31, described in Equation 32 as

$$T_s = \frac{c^2}{\gamma_d R_d} - 273.15, \tag{32}$$

where $\gamma_d = 1.4$ is the ratio of specific heats at constant pressure and volume and $R_d = 287.04$ J/(K-kg) is the universal gas constant. The sonic temperature, T_s, is an estimate of the true air temperature, but is also slightly sensitive to humidity fluctionations (since speed of sound also depends on humidity) [13].

The CSAT3 is able to take numerous point sonic temperature measurements at sample rates of up to 50 Hz. The amplitude and frequency of the temperature fluctuations are related to the turbulent eddy sizes that pass over the sensor. Large eddies produce large amplitude, low frequency fluctuations; smaller eddies produce lower amplitude, higher frequency fluctuations. Taking the power spectral density (PSD) of the temperature as a function of time should result in a plot looking like Figure 15, where a -5/3 slope is maintained over a certain frequency window on a log-log plot. This frequency window corresponds to the inertial subrange of Kolmolgorov turbulence. The refractive index structure parameter C_n^2 can be determined by the use of the -5/3 slope portion of the PSD, as shown schematically in Figure 15. At both ends of that diagram—the low frequency region (shaded pink) and the higher frequency region (shaded purple)— C_n^2 cannot be determined accurately because it either falls outside the intertial subrange or is

contaminated by the noise floor in those regions, respectively. C_n^2 prediction is more sensible in the inertial range (middle region), where the slope is approximately -5/3. At this point, C_n^2 can be expressed in terms of the sonic temperature structure parameter C_T^2 , as

$$C_n^{\,2} = A^2 C_T^{\,2}, \tag{33}$$

where $A(\lambda, P, T, q)$ is a function of the optical wavelength λ, the atmospheric pressure, P , the air temperature, T , and the specific humidity, q . The sonic temperature structure parameter C_T^2 is determined as

$$C_T^{\,2} = 4\left(\frac{2\pi}{U}\right)^{2/3} S_{T_S}(f)\, f^{5/3}, \tag{34}$$

where U is the mean wind speed, $S_{T_S}(f)$ the power spectral density of the sonic temperature and f is the frequency of the temperature fluctuations.

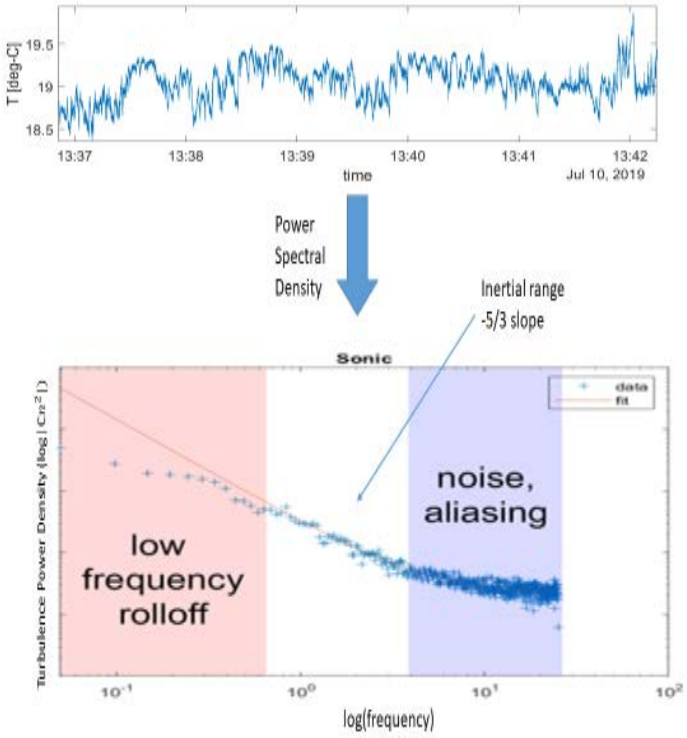

Figure 15. The upper plot shows an example of temperature versus time data from a sonic anemometer. Beneath that is a log-log plot of the power spectral density of the temperature data versus frequency, which is used to determine C_n^2, as explained in the text. Adapted from [3].

Additionally, rapid air temperature fluctuations can be measured by the use of a fine wire thermocouple that can be mounted to the side of the anemometer block, as shown in Figure 16. A fine-wire thermocouple (FWTC) consists of a pair of metal wires where each wire consists of a different metal. The principle of FWTC operation is based on the thermoelectic effect, where a voltage difference develops between the wires when there is a temperature gradient between the ends of the wires. The purpose of using the co-located FWTC is to provide an alternative method for measuring the temperature fluctuations (and thus C_n^2), for comparison with the sonic anemometer results.

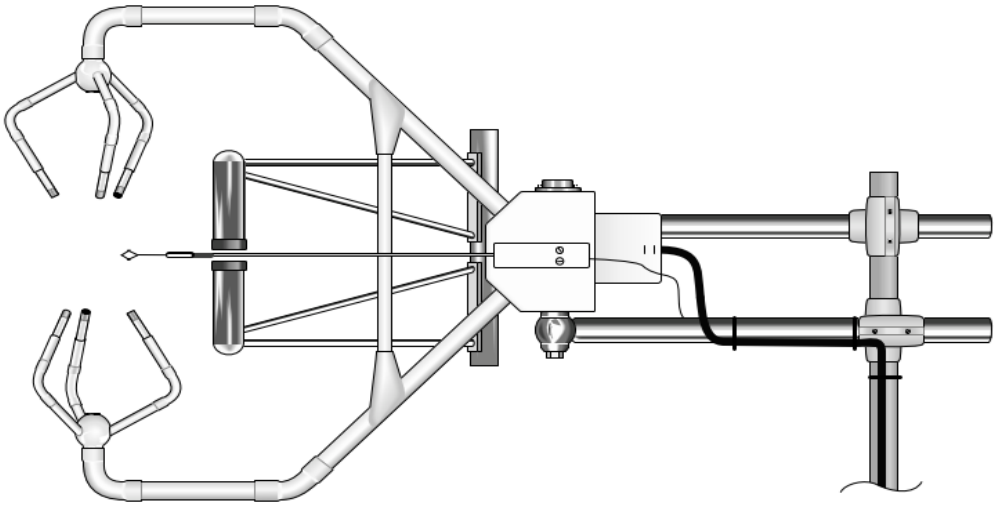

Figure 16. A fine wire thermocouple mounted to the side of the CSAT3 anemometer. Source: [13].

3. MZA DELTA Imaging Path Atmospheric Turbulence Monitor PM-02-600

The MZA DELTA Imaging Path Atmospheric Turbulence Monitor is used for measuring the atmospheric turbulence strength and profile over a line-of-sight optical path [14]. This DELTA system consists of the following individual parts, as shown in the Figure 17.

Figure 17. The MZA DELTA Imaging Path Atmospheric Turbulence Monitor PM-02-600.Source: [14].

- The Celestron f/10, 6-inch diameter aperture Schmidt-Cassegrain telescope. This telescope can be mounted on a tripod at a height about 0.91 to 1.3 meters off the ground [14].
- The Point Grey 3.2 mega-pixel, Grasshopper 3 USB Camera with 3.45 μm pixels. This camera can be mounted to the telescope and is used for aligning the telescope at the target and then collecting images of the target [14].
- A Data Acquisition Dell laptop computer which can collect measurement data through a USB cable connected to the above-mentioned camera [14].
- A DELTA target board with multiple checkerboard features placed at the opposing end of the optical path [14].

The DELTA software calculates turbulence over the desired optical path by tracking target board features as they jitter due to turbulence. Specifically, it measures

differential jitter of feature pairs as a function of angular separation. The C_n^2 turbulence profiles are estimated by observing the fluctuations over many length scales, where the cells close to the telescope (red box) are associated to larger scale fluctuations (differential jitter between widely-separated features, indicated by the red line on the target board image), while the cells close to the target board (green box) cause smaller scale fluctuations (indicated by the green line on the target board image), as shown in Figure 18.

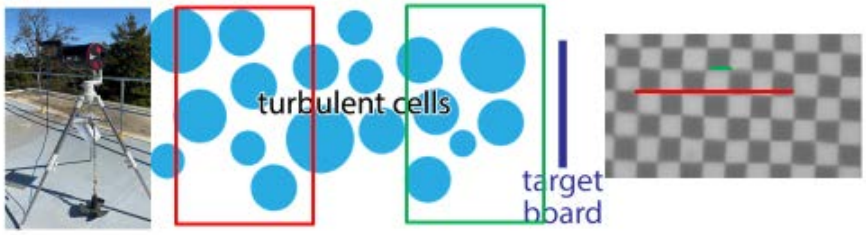

Figure 18. Differential jitter measurements vs. angular separation using MZA DELTA system. Source: [3].

Then, the DELTA system produces a data summary file which is updated based on the interval time of collecting data. Although the main output of the data summary file is the turbulence profile C_n^2, the DELTA system also provides the following set of useful propagation parameters:

- The measured profile of C_n^2 along the desired path [14].
- The Fried's spherical wave coherence diameter r_{0A} and r_{0B} from the perspective of the DELTA receiver and target board locations, respectively, at λ= 550 nm wavelength [14].

The results/plots of the DELTA data summary file can be used for further analysis, using wave-optics simulation tools [14].

B. EXPERIMENTAL SETUP

The experiment took place on the Monterey Bay area from 4 September 2020 through 28 October 2020. During this period, DELTA measurements were taken between two terminal stations, where the optical path distance was 1563 meters over the bay (see Figure 19) at height that varied from ~2.8 meters above the sea level at one end to ~10 meters at the other, though those values fluctuated due to tidal variation. At the same time, meteorological data was collected from the WS-2000 and a nearby NOAA weather station, located on the municipal pier.

Figure 19. The experiment location depicting the two terminal stations spaced 1563 meters apart

The DELTA measurements between the two terminal stations were supplemented with measurements from additional sensors on 18 September and 27–28 October 2020. On 18 September, two tripods were deployed, one of them on the CG pier, and the other onboard a NOAA ship (*R4017*) during its scheduled trip inside the Monterey Bay. The sensors installed on these tripods included CSAT3 sonic anemometers, in order to obtain

measurements of C_n^2 along the DELTA imaging path for comparison with the DELTA turbulence profiles. A FWTC was also installed on the tripod on the R4107, as an additional method for obtaining values of C_n^2. On 27 and 28 October, one tripod was deployed onboard a NOAA ship (*Fulmar*) during its trip over the Monterey Bay which took place outside of the DELTA imaging path. On those days of the experiment, a FWTC and the WS-2000 sensor were also installed on the tripod on board the *Fulmar*. These experiments will be described in more detail below.

The meteorological data collected by the WS-2000 and the NOAA weather station was incorporated into NAVSLaM to predict C_n^2 values at different heights; these predictions were compared to both DELTA and CSAT 3 C_n^2 measurements. The following sections describe the locations of each sensor placement:

1. Coast Guard Pier

The Monterey Coast Guard (CG) Pier was the location of the DELTA receiver (telescope), which was installed on the pier itself and looking across the bay to the target board. The WS-2000 weather station was also installed on the CG pier at height of ~4.8 meters above sea level, providing meteorological data such as air temperature, relative humidity, air pressure, wind speed, solar radiation and rainfall rate. Moreover, an additional weather sensor operating by National Oceanic and Atmospheric Administration (NOAA) and located at the Monterey Municipal Pier was used, providing additional measurements, including sea temperature, which was not possible to be provided by the WS-2000.

Figure 20. The DELTA sensor as well as the WS-2000 weather station set up at the CG Pier

2. DELTA Target Location

The DELTA target was located on a coastal bluff above the Monterey Bay, on Navy property, at a distance of 1563 meters southeast of the CG pier, as shown in figures 19 and 21.

Figure 21. The DELTA target board

3. Combined Measurements of DELTA and Other Sensors during NOAA Boat Excursions

The experimental measurements at sea were carried out in two different periods, as given in the sections that follow.

a. NOAA Boat (R4017) Excursion on 18 September 2020

Two CSAT3 sonic anemometers and other sensors were deployed on 18 September 2020 to operate simultaneously with the DELTA system, supplementing the experimental measurements along the optical path of the DELTA.

One of the sonic anemometers equipped with a FWTC was installed on NOAA R4017 ship's bow at a height of 3.8 meters above the sea level, while the other sonic anemometer was set up (without a FWTC) at the CG Pier in front of the DELTA system at a height of ~4.2 meters above the sea level, as they are shown in Figure 22.

Figure 22. The CSAT3 sonic anemometers at the CG Pier (left) and on-board NOAA ship (*R4017*) (right).

The NOAA vessel was instructed to stop at 4 waypoints (WP) spaced about 300 meters apart along the optical path of the DELTA, as shown in Figure 23. The boat stopped for at least five minutes at each WP, allowing the sonic anemometer and thermocouple to record sufficient measurements. Ultimately, both sonic anemometers were able to operate simultaneously with the DELTA sensor for 1 hour and 30 minutes. The deployment of the NOAA vessel as a midway station between the two terminals was able to happen for only one day during the experimental period due to limited availability of such vessels to support the experimental purpose. Moreover, due to the poor availability and rapid degradation of FWTCs, the use of them was limited and implemented only on the sonic anemometer on board the vessel when that vessel was deployed.

Figure 23. NOAA vessel (R4017) was assigned to move towards and stop in the vicinity of the depicted four WP's

b. During NOAA Boat (Fulmar) Excursion on 27 and 28 October 2020

One sonic anemometer, equipped with a FWTC, was installed on NOAA *Fulmar* ship's bow at a height of 3 meters above the sea level. During that excursion, the WS-2000 weather station sensor was mounted on the same tripod as the sonic anemometer, as shown in Figure 24, in contrast to the *R4017* excursion, where the WS-2000 was installed on CG

Pier. Furthermore, contrary to the 18 September experimental trip, there was no need for using an additional sonic on the CG Pier, as the *Fulmar* trip took place outside of the DELTA imaging path.

Figure 24. The CSAT3 sonic anemometer, with the WS-2000 mounted on top of it, on-board NOAA (*Fulmar*) ship

The track that the *Fulmar* followed in the Monterey Bay during the experimental period of 27 and 28 October 2020 is depicted in Figure 25.

Figure 25. NOAA vessel (Fulmar) track over the Monterey Bay

THIS PAGE INTENTIONALLY LEFT BLANK

V. EXPERIMENTAL ANALYSIS

In this chapter, a thorough analysis is provided about the turbulence fluctuations in a maritime environment for the experimental campaigns described in Chapter IV.

A. C_n^2 COMPARISON BETWEEN METHODS

The experimental analysis begins by studying and comparing the C_n^2 turbulence profiles predicted by the CSAT3 sonic anemometer and a fine-wire thermocouple (FWTC) on board NOAA ships as well as the C_n^2 turbulence profile predicted by NAVSLaM using the meteorological data collected by the WS-2000 and NOAA weather stations during the sea experiments. Also, the DELTA profile will be compared to the predictions from NAVSLaM.

1. Comparison between CSAT3 Sonic Anemometer, Fine-Wire Thermocouple, and NAVSLaM C_n^2 Turbulence Profiles

a. Sea Experiment Analysis during NOAA boat (R4017) Excursion on 18 September 2020

Figure 26 illustrates the C_n^2 turbulence values provided by the sonic anemometer CSAT3 (blue curves) and the FWTC (orange curves) mounted on board the NOAA vessel. The CSAT3 was set up on board the boat at a time around 1450 the day before the sea experiment (on 17 September), while the FWTC was installed on the tripod (collocated with the CSAT3) around 0910 on 18 September, approximately 80 minutes before the start of the sea experiment.

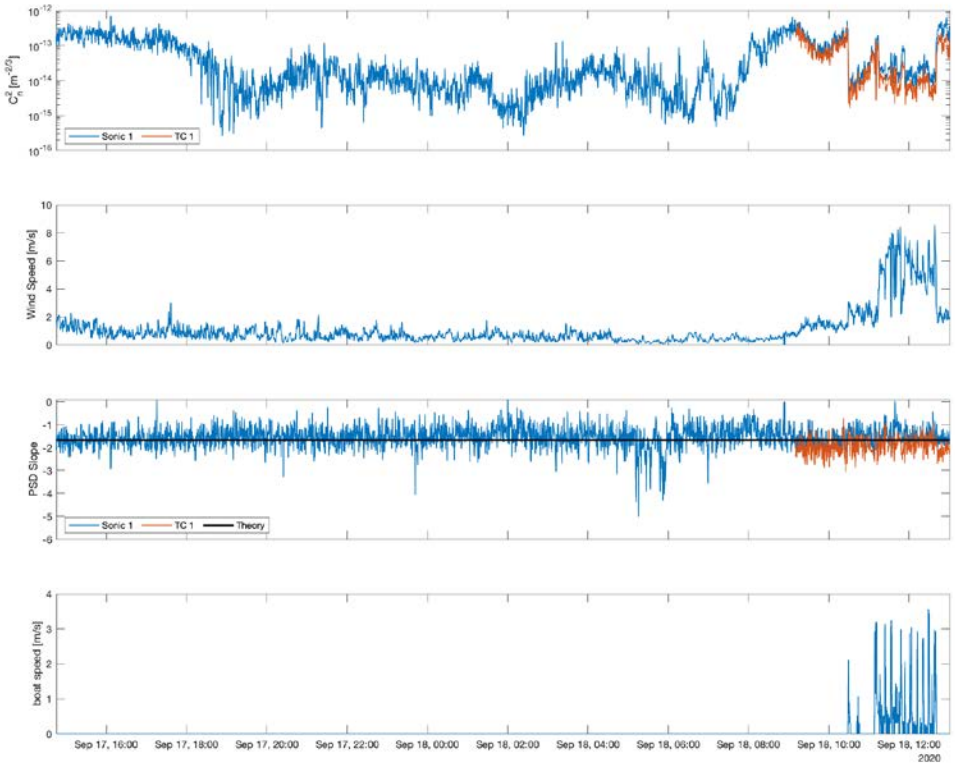

Figure 26. The refractive index structure parameter C_n^2 given by sonic anemometer and thermocouple sensors, the wind speed, the PSD slope and the boat speed plots over time for the R4017 excursion

An overall analysis of C_n^2 turbulence values (see top plot of Figure 26) shows the following trends:

- The greatest values of C_n^2 are from late afternoon hours until sunset (at 1850) of 17 September, likely due to the solar heating of the ship's deck and the air above it.
- After sunset and during overnight hours the value of C_n^2 fell noticeably, although it fluctuated quite a bit. The reduced turbulence levels are likely due to the temperature of the ship's deck and the air above it becoming more similar. Since the C_n^2 estimates from the CSAT3 assume turbulent air cells are

flowing over the sonic anemometer, when the wind speed is low (much less than 1 m/s) the C_n^2 values may be less accurate. This is reflected in the slope of the PSD plot (third plot from the top), which deviates from -5/3 around 0600 on 18 September when the wind speed is very low.

- As expected, an upward trend in C_n^2 appeared from sunrise (at 0650) until around 0900 of 18 September, as the sun was starting to heat the ship's deck and the air above it again. After that time period and until the ship's departure, the C_n^2 values remained almost steady at strong turbulence levels, displaying only some small fluctuations.

- Once the NOAA vessel departed the CG Pier at 1030, C_n^2 dropped sharply, as the sensors began to sample more of the marine air and was less affected by the warm air above the ship's deck. It is during these times that the measured turbulence is likely a more realistic measure of the maritime environment.

- While the boat was underway, some occasional sharp fluctuations were observed. These fluctuations may be due to the boat stopping at the waypoints (WPs) (see bottom plot of Figure 26) ; when it slowed down or stopped, the turbulence again became more affected by the warm air above the boat's deck.

- Finally, C_n^2 sharply increased again to the original strong turbulence levels when the boat returned to the CG Pier.

As described in the previous chapter, the PSD of the temperature fluctuations should produce a -5/3 slope on a log-log plot within a certain frequency window corresponding to the inertial subrange. The third plot of Figure 24 shows the slope of the best fit line to the PSD within 1 Hz and 5 Hz for both the CSAT3 data (blue line) and (when deployed) the thermocouple data (red line).

Focusing the analysis more on the time period when the R4017 was deployed (see Figure 27), the following conclusions are drawn:

- The C_n^2 sonic anemometer and thermocouple measurements agree well, especially in the beginning of the experiment as shown in the top plot of Figure 27. However, starting at about 1115, the thermocouple's measurements produced smaller values of C_n^2 than the CSAT3, while maintaining the same overall pattern. That offset is hypothesized to be due to the wire thermocouple's rapid degradation due to environmental conditions (for instance, saltwater deposits on the thermocouple could affect its measurements).

- A distinguishable change in the C_n^2 values can be seen at time 1030 when the ship left the pier. During the time period when the NOAA vessel was at the CG Pier, the C_n^2 values obtained by the sensors appeared to be pretty smooth, without extreme low or high peaks, showing a mean C_n^2 value of about $9\times10^{-14}m^{-2/3}$ at the location of the sensors. However, once the vessel departed the CG pier, the C_n^2 value underwent a significant drop, with a mean C_n^2 value of about $2\times10^{-14}m^{-2/3}$ along the entire pathway.

- The C_n^2 values during the ship excursion were quite variable, with obvious high and low peaks potentially caused by the ship's varying speed relative to the prevailing wind speed at sea, taking into consideration the ship's frequent stops at WPs along the optical path, as shown in the bottom plot of Figure 27.

- The PSD slope was less than -5/3 when the boat was docked at the CG pier, with the smallest values occurring during the early morning hours—between 0430 and 0700—of 18 September 2020, where the wind speed magnitude was closed to zero. That makes sense, as the low wind speed may yield unreliable measurements of the sonic anemometer, as previously described. During the sea experiment, as expected, the slope mostly fluctuated near -5/3; when the boat left the pier and started developing speed, the effective wind speed across the sensors increased, so the sonic anemometer could more accurately sample the turbulent fluctuations over the water. However, the slope was not constant during the whole experiment, as there were points where the slope was flatter

(greater than -5/3) because of noise contamination possibly caused by intense vibrations or strong wind gusts.

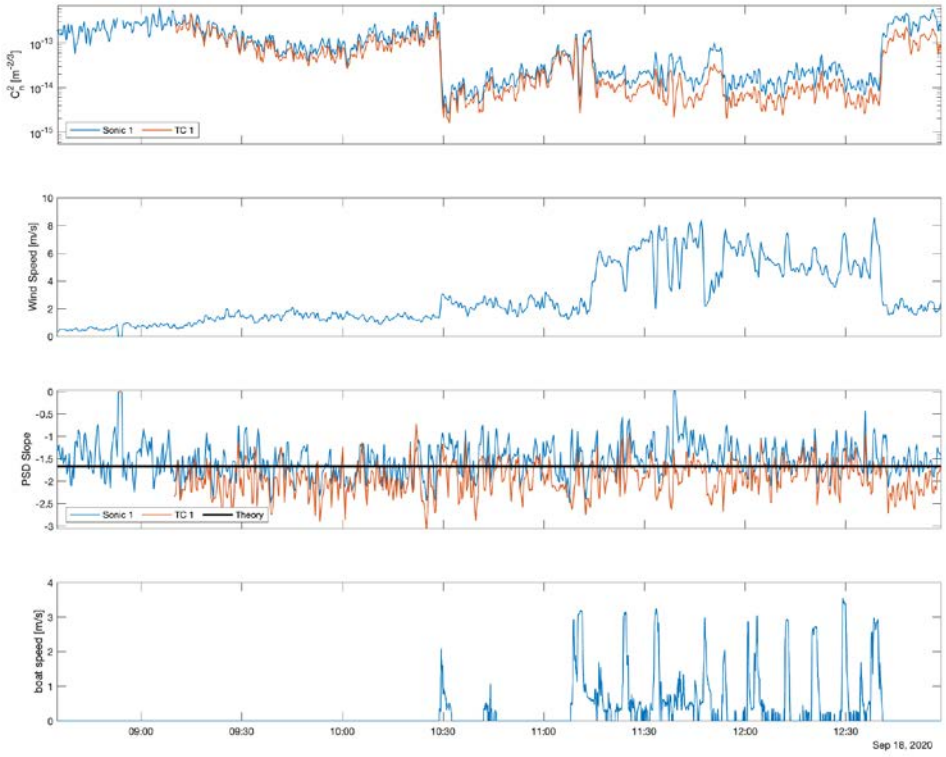

Figure 27. A zoomed-in plot of the underway experiment period of Figure 24, including the boat speed over time plot

In addition to the above mentioned experimental results, the meteorological parameters measured by the WS-2000 and NOAA weather stations were processed via NAVSLaM to estimate the C_n^2 value at the height of the sensors (3.8 meters above the water). The parameters (see figures 28 and 29) needed by NAVSLaM to run were the following:

- The optical wavelength set at 1.5 μm.

- The wind speed provided by the WS-2000, which was slightly (about 1–2 m/s) lower compared to the wind speed measured by the sonic anemometer, during the experiment at sea. That difference was due to the boat motion and the fact that the WS-2000 was not co-located with the boat.

- The air temperature provided by the WS-2000, which increased significantly during the sea experiment (by about 2.5°C).

- The sea surface temperature provided by the NOAA weather station, which fluctuated over a smaller range (about 0.5 °C) during the sea experiment, in contrast to the air temperature.

- The relative humidity and the atmospheric pressure provided by the WS-2000, both of which also dropped during the sea experiment, but they have less effect on C_n^2.

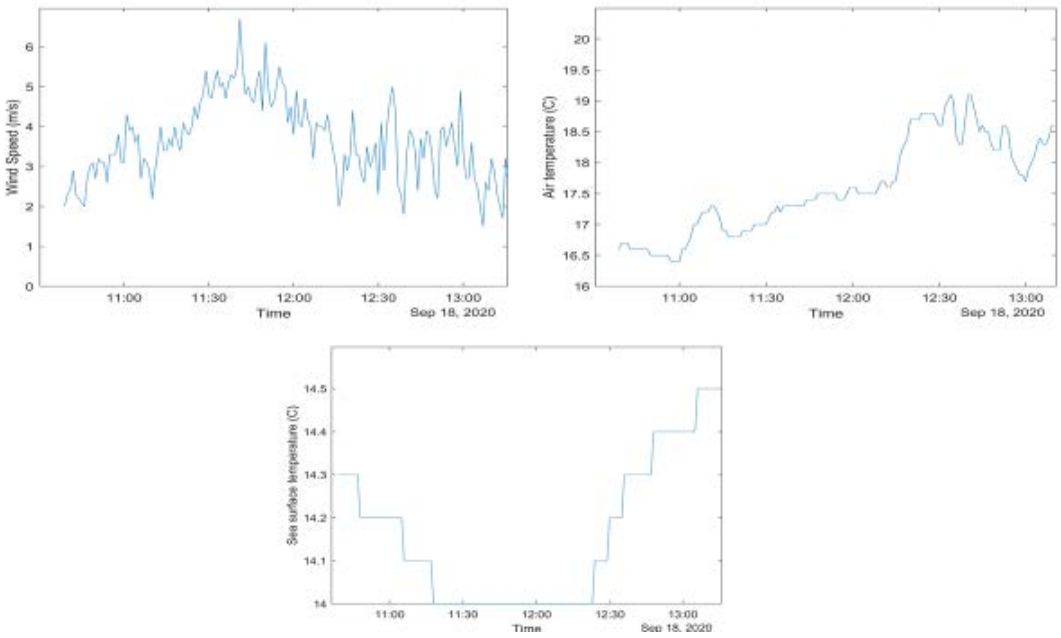

Figure 28. Meteorological parameters (wind speed, air temperature and sea surface temperature) plots over time for the R4017 excursion

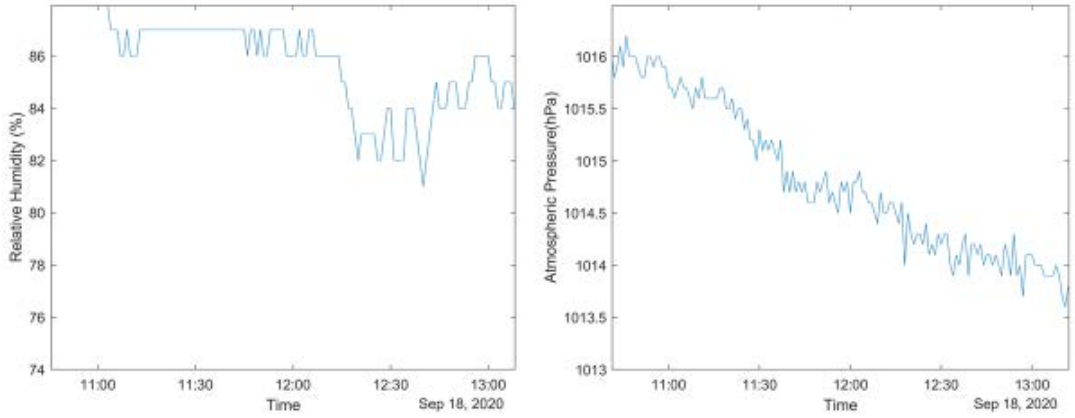

Figure 29. Meteorological parameters (relative humidity and atmospheric pressure) plots over time for the R4017 excursion

Figure 30 presents a comparison between the C_n^2 turbulence values obtained by the CSAT3 (and the thermocouple mounted on it) and predicted by NAVSLaM during the time the ship was deployed. It is noticed that NAVSLaM obtains roughly the same order of magnitude as the measurements while the boat was underway, suggesting that NAVSLaM is a useful model for getting an order-of-magnitude estimate of the turbulence over the water. When the boat returned to the CG Pier (around 1245), NAVSLaM disagreed significantly with the sonic anemometer and thermocouple values, but that was not surprising due to the warm air over the boat greatly affecting C_n^2 values.

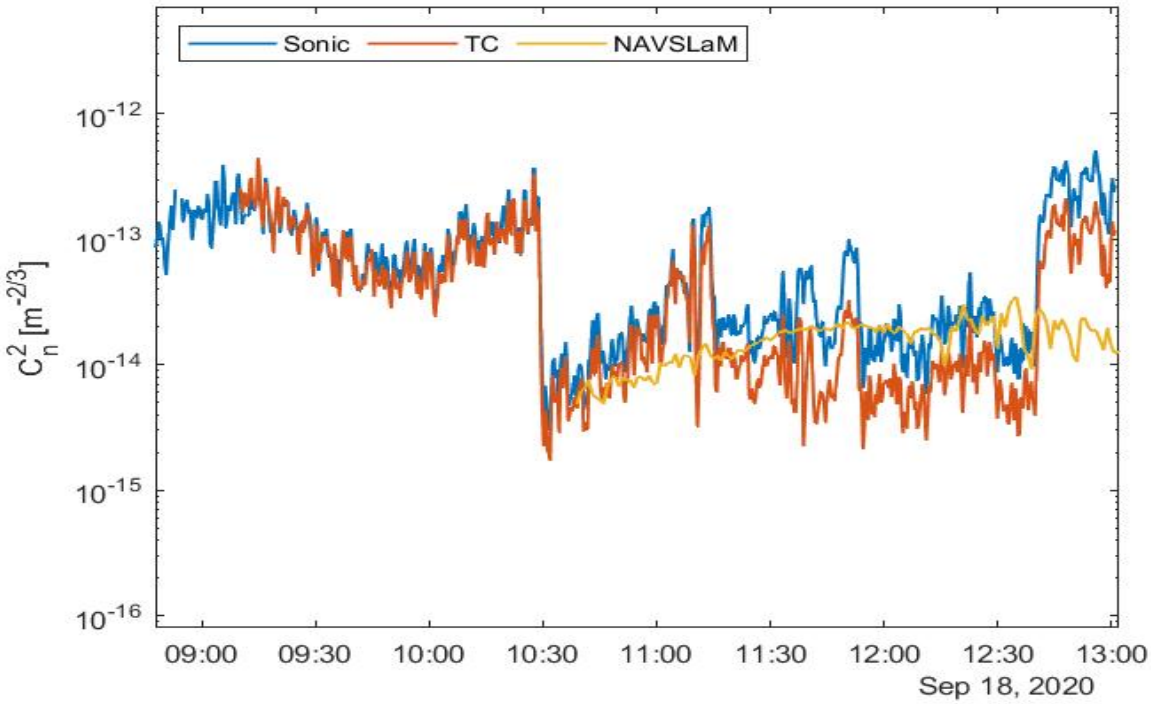

Figure 30. The refractive index structure parameter C_n^2 versus time for the sonic anemometer and thermocouple sensors, compared to predictions from NAVSLaM for the R4017 excursion

b. Sea experiment analysis during NOAA boat (Fulmar) excursion from 26 to 27 October 2020

Figure 31 presents the turbulence values provided by the sonic anemometer CSAT3 and the fine wire thermocouple mounted on board the *Fulmar*. The CSAT3 was set up on board the boat around 1700 on 26 October, while the thermocouple was installed on the tripod (collocated with the CSAT3) around 0650 on 27 October, about one hour before the boat's departure from the pier.

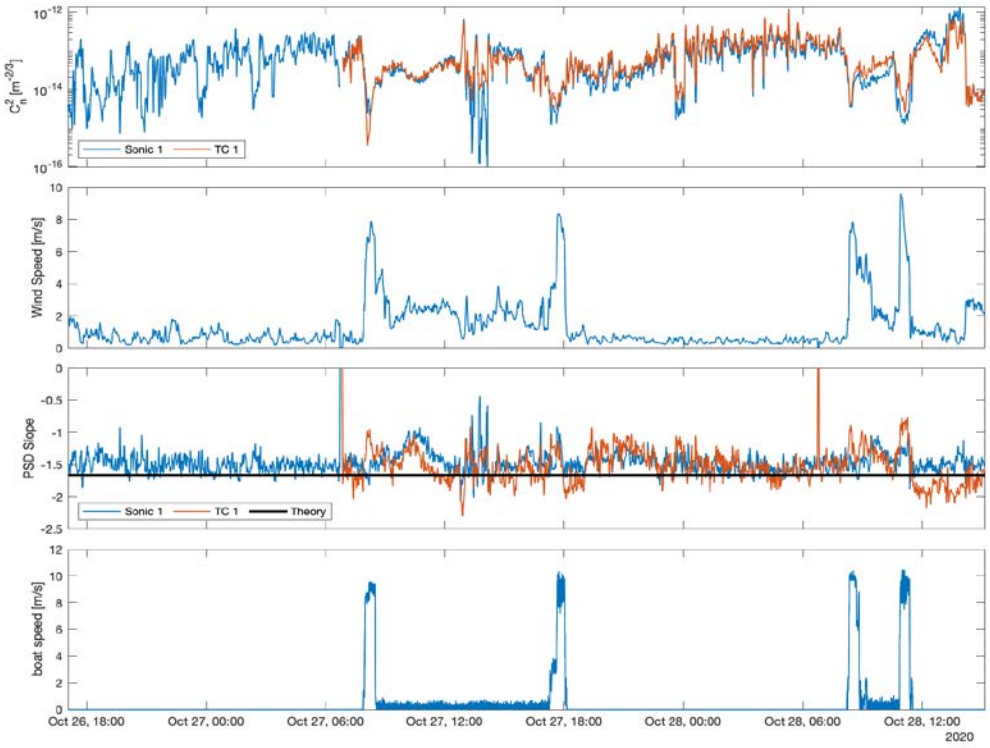

Figure 31. The refractive index structure parameter given by sonic anemometer and thermocouple sensors, the wind speed, the PSD slope and the boat speed plots over time for the Fulmar excursion

Figure 31 shows plots of C_n^2 from the CSAT3 and thermocouple (determined in a manner similar to before), as well as the indicated air speed across the sonic, slope of the PSDs, and boat speed. The following are trends regarding the C_n^2 turbulence values:

- The period before the thermocouple was installed on the sonic anemometer, while the NOAA vessel was at the CG Pier, the C_n^2 appears to fluctuate from about 10^{-13} $m^{-2/3}$ to 10^{-15} $m^{-2/3}$, possibly due to changing wind directions and influence of airflow from the pier and boat. However, from the early morning hours until the boat departure, the turbulence remains at stronger levels, i.e. $C_n^2 \approx 10^{-14}$ $m^{-2/3}$.

- A distinct spiky artifact in the PSD slope is noticed just before the boat's departure due to replacing the batteries and the thermocouple installation on the sonic tripod.

- Sonic anemometer and thermocouple C_n^2 values appear to be correlated pretty well, except for the last few hours of the 28 October sea experiment. That makes sense if we assume degradation of the thermocouple after some time period from its first use, as may have also happened during the sea experiment of 18 September described in the previous section.

- A sharp drop in C_n^2 occured once the vessel begin to deploy during both 27 and 28 of October sea experiments, since the sensors began to sample more of the marine air and thus were less affected by the air above the ship's deck.

- When the vessel reached its desired station, it nearly stopped between 0835 to 1235 of 27 October. During that time, the C_n^2 values were generally steady, with some small fluctuations possibly due the wind direction changing. However, we observe a considerable amount of fluctuations in C_n^2 values provided by the sonic between 1230–1430 of 27 October. During that period, we also notice that the PSD slope (see third plot of Figure 31) deviated from the theoretical -5/3 value, especially for the CSAT3, possibly due to shipboard vibrations. The thermocouple readings, which are not affected by vibrations, also fluctuate during this time, but not as extremely as those readings from the CSAT3.

- While the vessel was again at the CG Pier, between 1800 of 27 October and 0800 of 28 October, the C_n^2 values appeared to be rather steady, showing again some sporadic fluctuations due to influence of air flow from the deck and pier.

- The pattern is similar for the 28 October sea experiment. The C_n^2 values drop when the boat develops speed so that the sensors begin to sample more of the marine air.

Focusing on the PSD slope (see third plot of Figure 31), the following remarks can be drawn:

- Overall, both sonic anemometer and thermocouple measurements seems to follow the theoretical -5/3 PSD slope pretty well except for the last time region of 28 October, where the thermocouple measurements profile fluctuates strongly with respect to the -5/3 slope. This may indicate, as mentioned previously, that the thermocouple performance was degraded during that time, possibly due to salt deposition on the sensor.

- While the boat was underway, the slope fluctuated near the theoretical value of -5/3, as expected, since the effective wind speed across the sensors increased allowing the sonic anemometer to more accurately sample the turbulent eddies over the water.

The meteorological parameters measured by the WS-2000 and NOAA weather stations were processed via NAVSLaM to estimate the C_n^2 value at the height of the sensors (3 meters above the water). The parameters (see figures 32 and 33) needed by NAVSLaM to run, as described in the previous section as well, were the following:

- The optical wavelength set at 1.5 μm.

- The wind speed provided by the WS-2000, which was about the same as the wind speed measured by the sonic anemometer, during the experiment at sea. For most of the recording period, the ship was relatively motionless, and hence the measured wind speed should roughly equal the true wind speed.

- The air temperature provided by the WS-2000, which appears to be increased during the daytime from 6° C to 12° C, as expected.

- The sea surface temperature provided by the NOAA weather station, which fluctuated over a general small range of about 0.6°C, in contrast to the air temperature.

- The relative humidity and the atmospheric pressure provided by the WS-2000, which were lower during the sea experiment. However, these meteorological parameters have less effect on C_n^2.

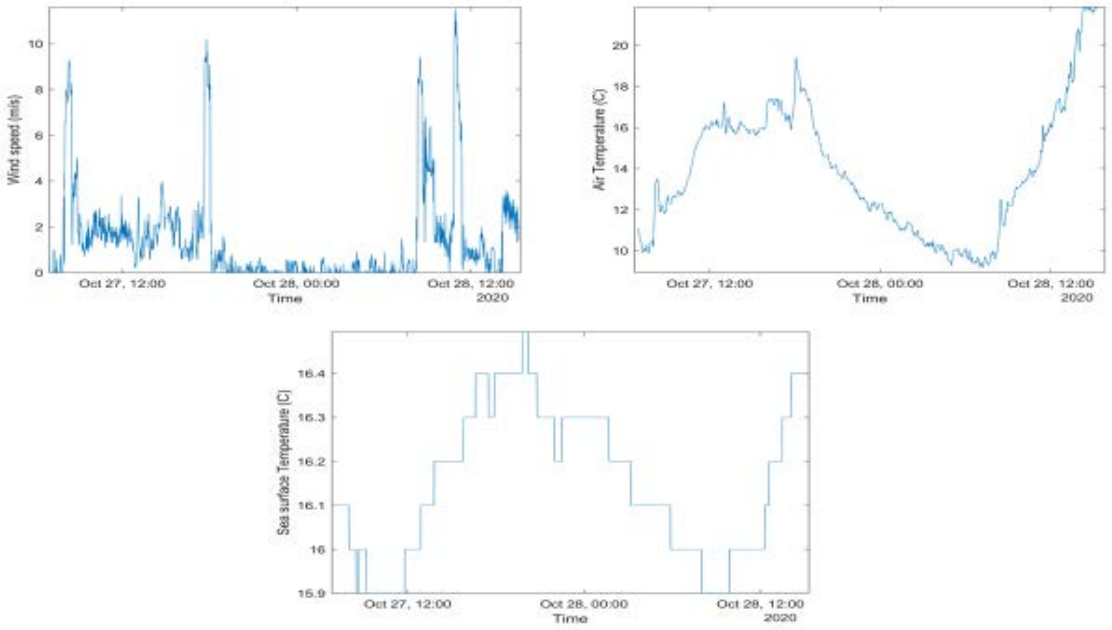

Figure 32. Meteorological parameters (wind speed, air temperature, and sea surface temperature) over time for the Fulmar excursion

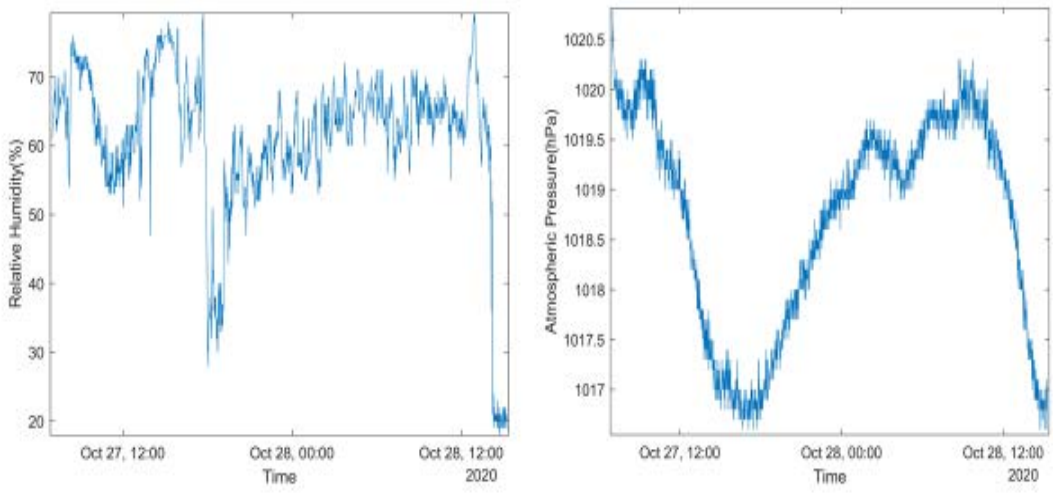

Figure 33. Meteorological parameters (relative humidity and atmospheric pressure) over time for the Fulmar excursion

Figure 34 presents a plot for the C_n^2 turbulence values obtained by the CSAT3 and the co-located thermocouple, along with the NAVSLaM model predictions, during the time the ship was deployed. Overall, although the NAVSLaM curve seems to follow roughly the same trend as the sonic and thermocouple plots, there is obviously an offset between them, where the NAVSLaM model indicates weaker C_n^2 turbulence than the values provided by the other sensors. Perhaps that is due to the difference in water temperature between the measured location (near the shore) and the boat's position a few kilometers from the shore (it is the air-sea temperature difference that is a large driver of turbulence near the surface). Also, during the night when the boat has returned to the dock, the sonic and thermocouple are more influenced by the presence of the boat, hence the larger differences during this time.

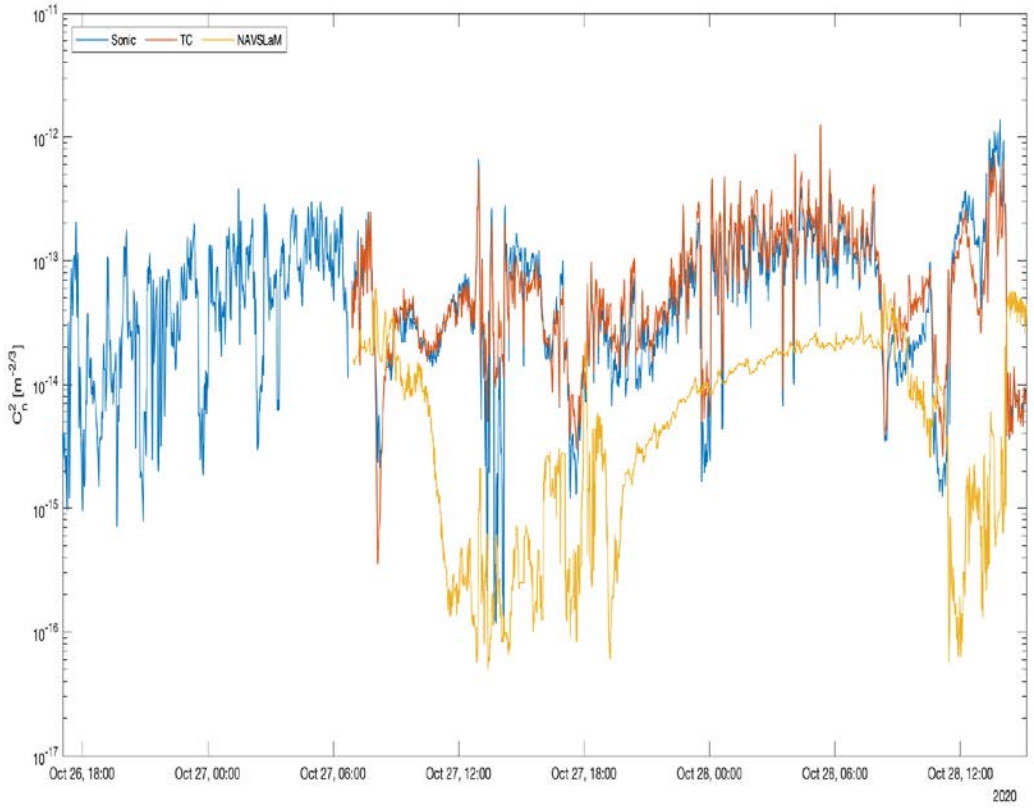

Figure 34. The refractive index structure parameter versus time for the sonic anemometer and thermocouple sensors, compared to predictions from NAVSLaM for the Fulmar excursion

2. Comparison between DELTA and NAVSLaM C_n^2 Turbulence Profiles

Figures 35 through 47 present the comparative plots between C_n^2 turbulence values, from 4 September 2020 through 26 October 2020, obtained by the DELTA sensor and estimated from NAVSLaM. The plots provided by the DELTA are generated in such a way as to meet the following conditions:

- There was more than 60 minutes of DELTA data on each day.
- There were greater than five samples of DELTA data with C_n^2 confidence level greater than 90% per hour. The C_n^2 confidence level depends on the number of

the highest confidence gradient pixels from the total number of the extracted gradient pixels of the target image.

The shaded area on the plots represents the 68% scattering interval of the DELTA sensor. That means that 68% of the C_n^2 values for the DELTA reside within that shaded area for each hour, giving an indication on how much variation in C_n^2 was measured at each location over the course of an hour. The blue squares and the red line on the plots characterize the mean C_n^2 values from the DELTA and NAVSLaM, respectively, along the optical path over each specific hour. In the figures, distance 0 marks the location of the DELTA receiver on the CG Pier. The DELTA was programmed to provide C_n^2 estimates along ten bins equally spaced from the receiver to the target board located 1563 meters away (see Figure 19). NAVSLaM processed the meteorological parameters measured by the WS-2000 and NOAA weather stations to estimate the C_n^2 value at the height of the sensors along the optical path (i.e., about 3 meters above the water), taking into account the tidal variations as well.

An overall analysis of DELTA and NAVSLaM profiles yields the following trends:

- Both DELTA and NAVSLaM profiles show that they agree within an order of magnitude during the whole experiment, except for two days (10 and 16 September) where there is an obvious inconsistency of the two profiles.
- The ideal situation, where the NAVSLaM line falls exactly within the shaded area, is noticed only on certain days (5, 15, 17, 18 September) of the experiment.
- The NAVSLaM profile is generally higher closer to the receiver. This is because the DELTA telescope on the CG pier was closer to the surface than the target. Turbulence is generally stronger near the surface due to greater convection and wind shear near the surface.

The variations between DELTA and NAVSLaM profiles could be due to the following reasons:

- Erroneous DELTA measurements that could be due to CG Pier vibrations and / or marine vessel traffic along the image path.

- Inaccurate meteorological data provided to NAVSLaM that could be due to the different locations of the WS-2000 and NOAA weather stations.

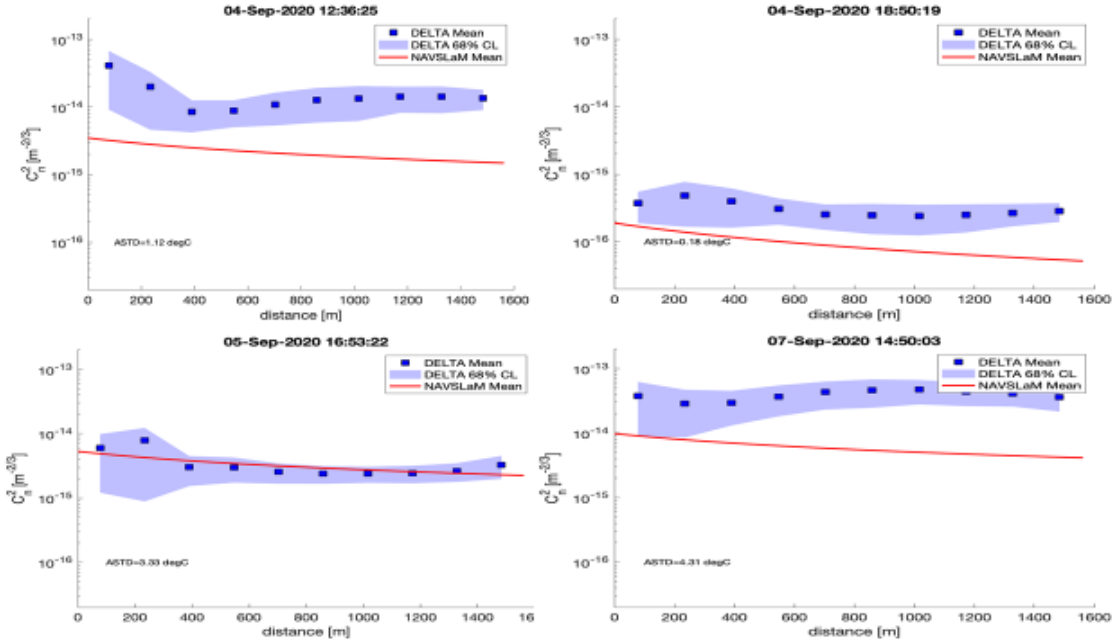

Figure 35. Comparative plots between DELTA and NAVSLaM provided profiles for 4, 5, and 7 September 2020

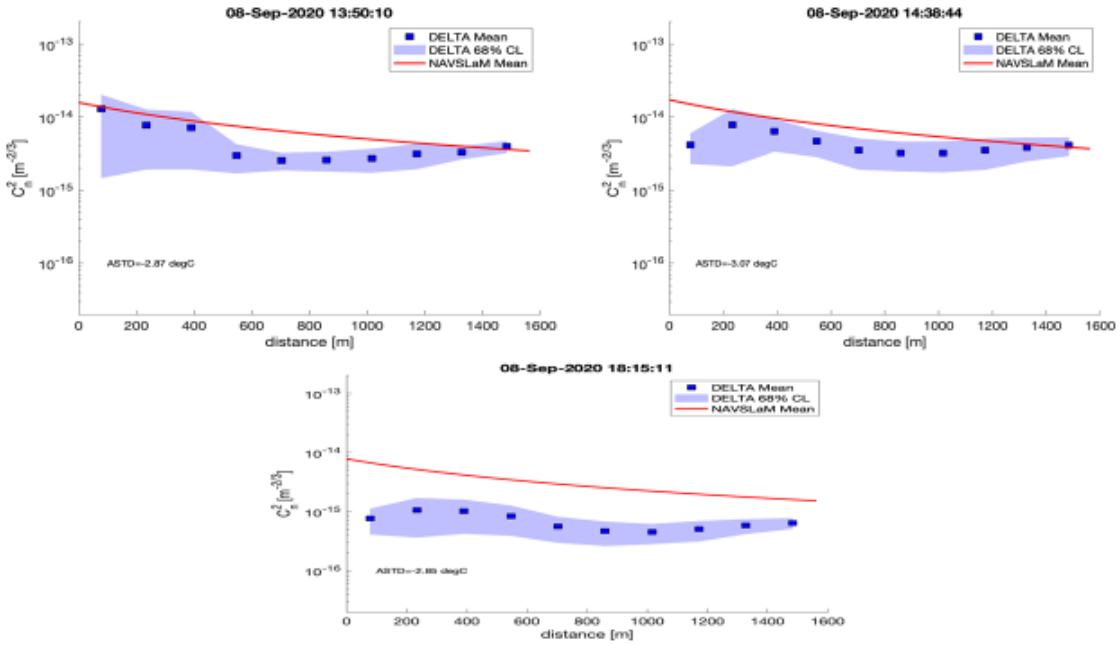

Figure 36. Comparative plots between DELTA and NAVSLaM provided profiles for 8 September 2020

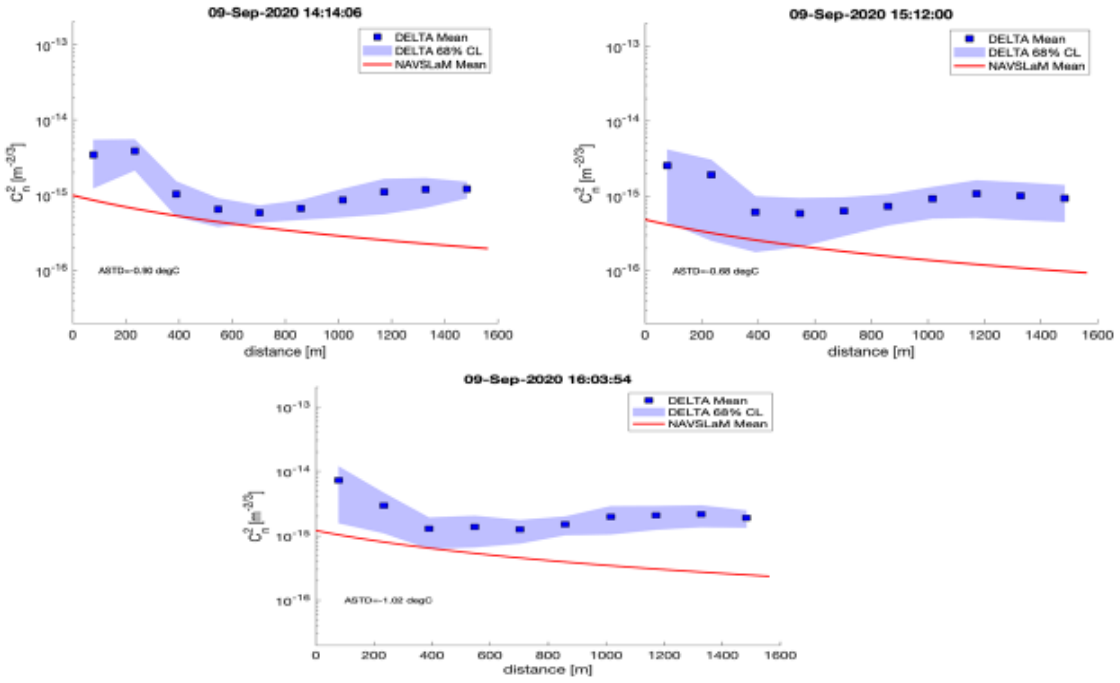

Figure 37. Comparative plots between DELTA and NAVSLaM provided profiles for 9 September 2020

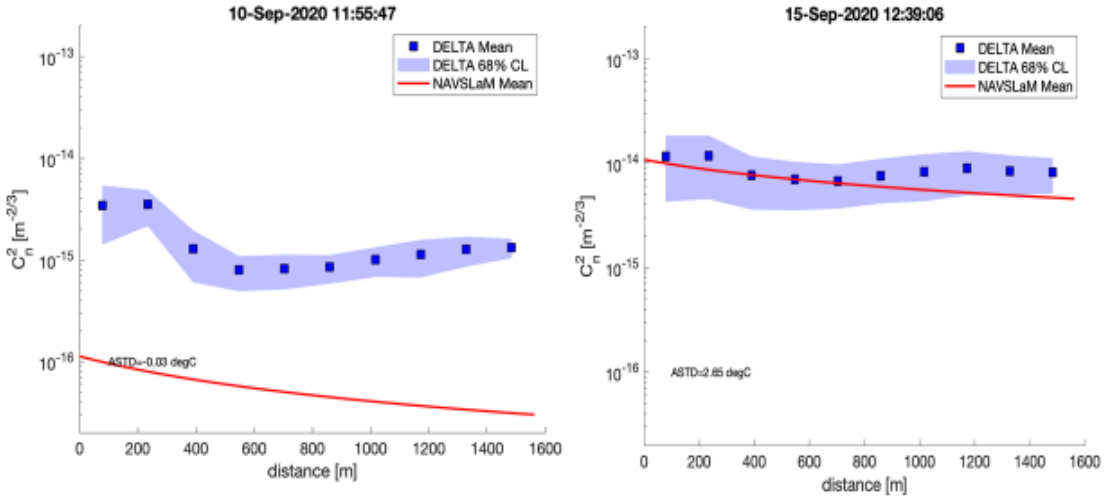

Figure 38. Comparative plots between DELTA and NAVSLaM provided profiles for 10 and 15 September 2020

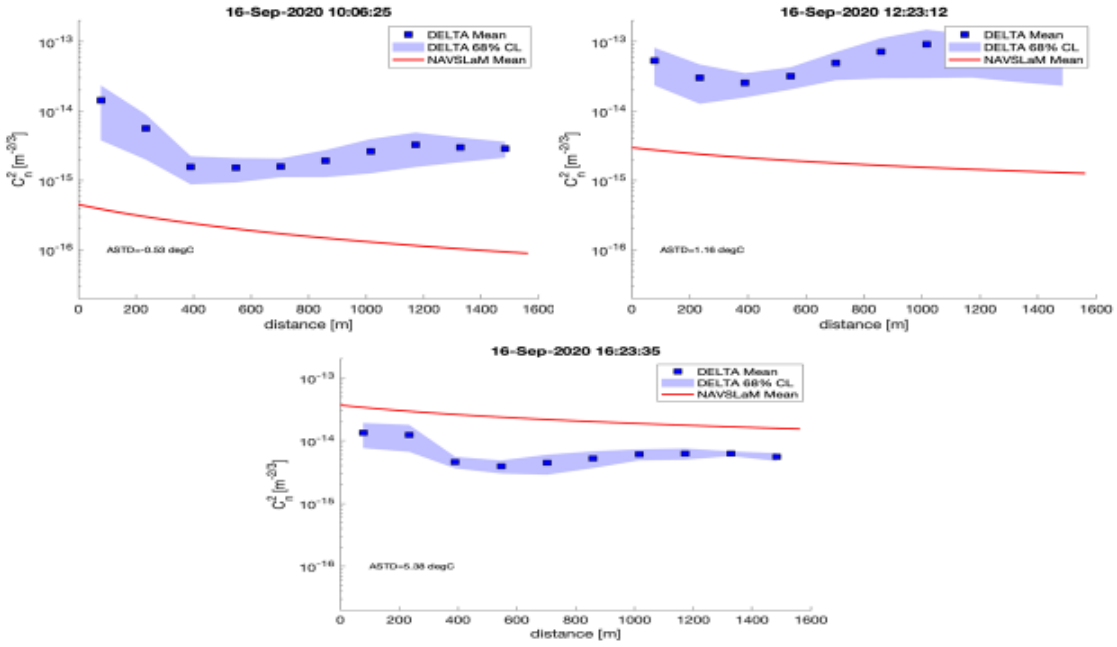

Figure 39. Comparative plots between DELTA and NAVSLaM provided profiles for 16 September 2020

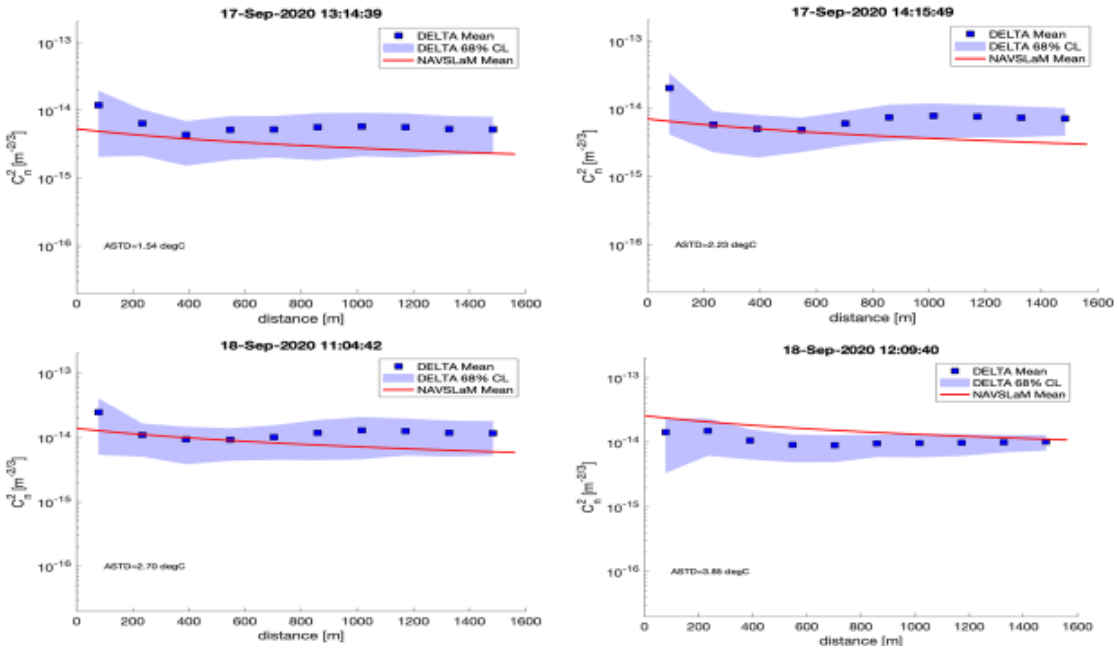

Figure 40. Comparative plots between DELTA and NAVSLaM provided profiles for 17 and 18 September 2020

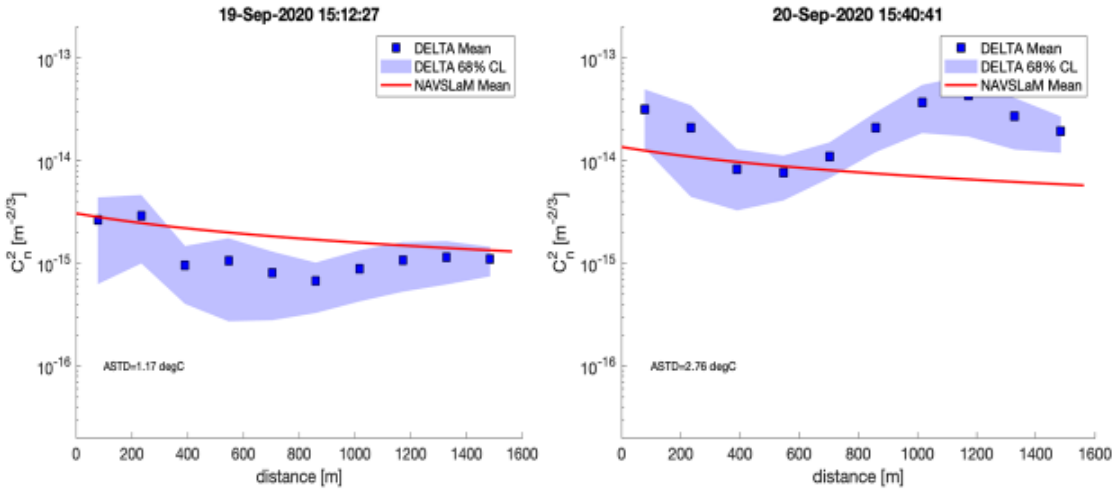

Figure 41. Comparative plots between DELTA and NAVSLaM provided profiles for 19 and 20 September 2020

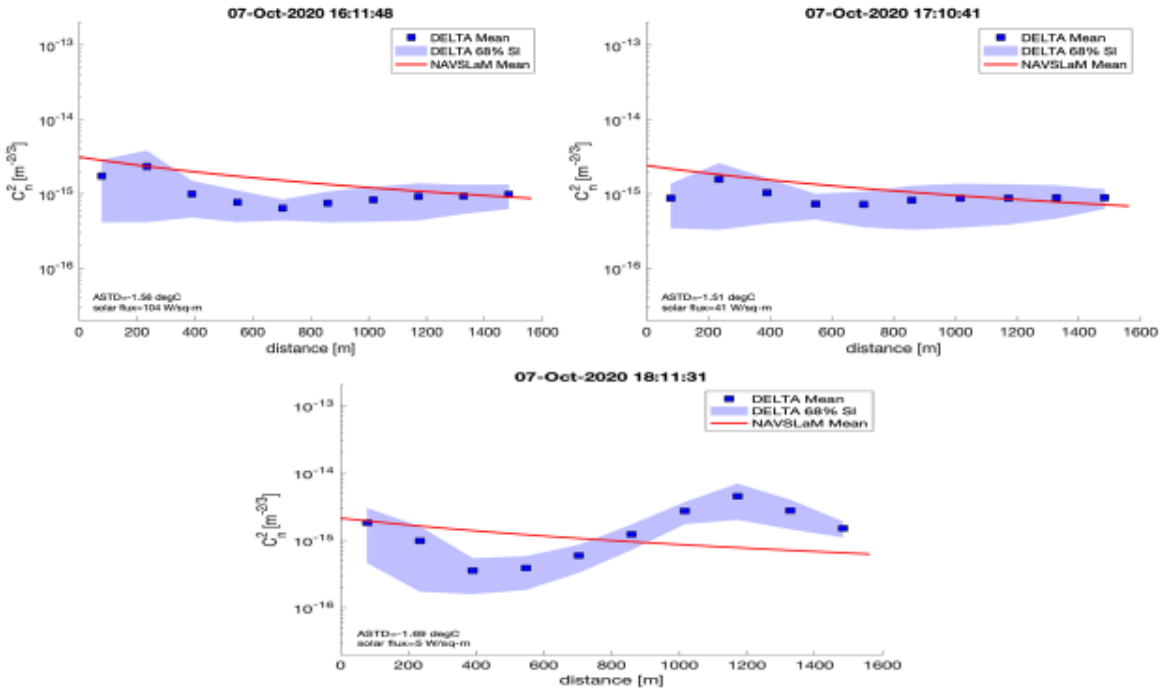

Figure 42. Comparative plots between DELTA and NAVSLaM provided profiles for 7 October 2020

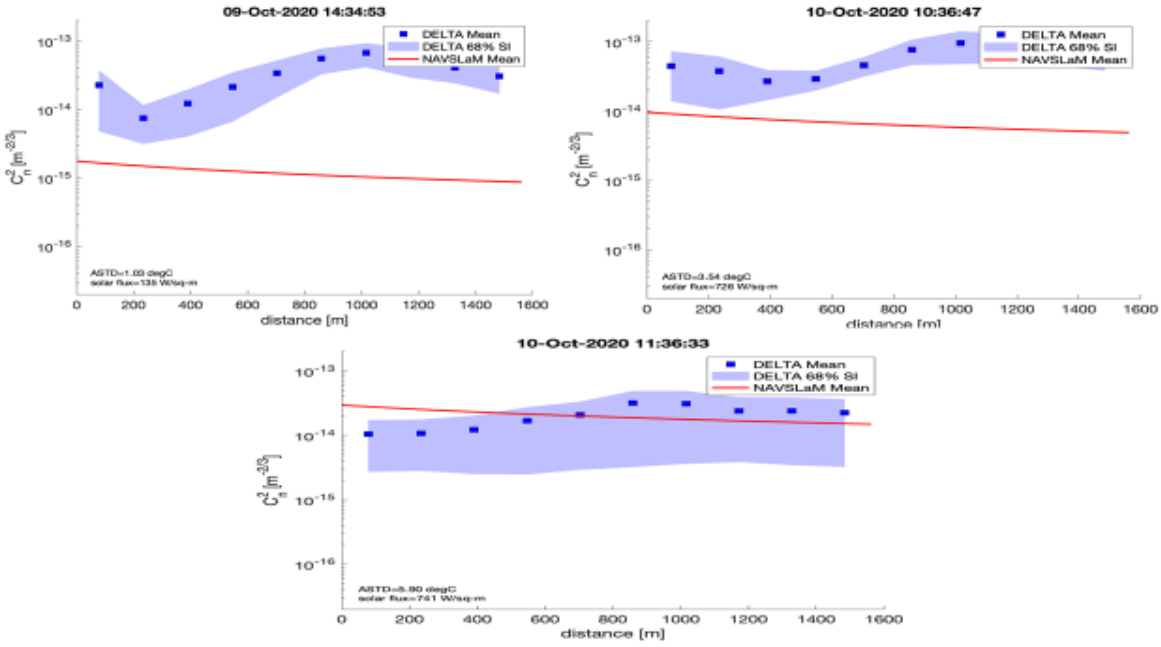

Figure 43. Comparative plots between DELTA and NAVSLaM provided profiles for 9 and 10 October 2020

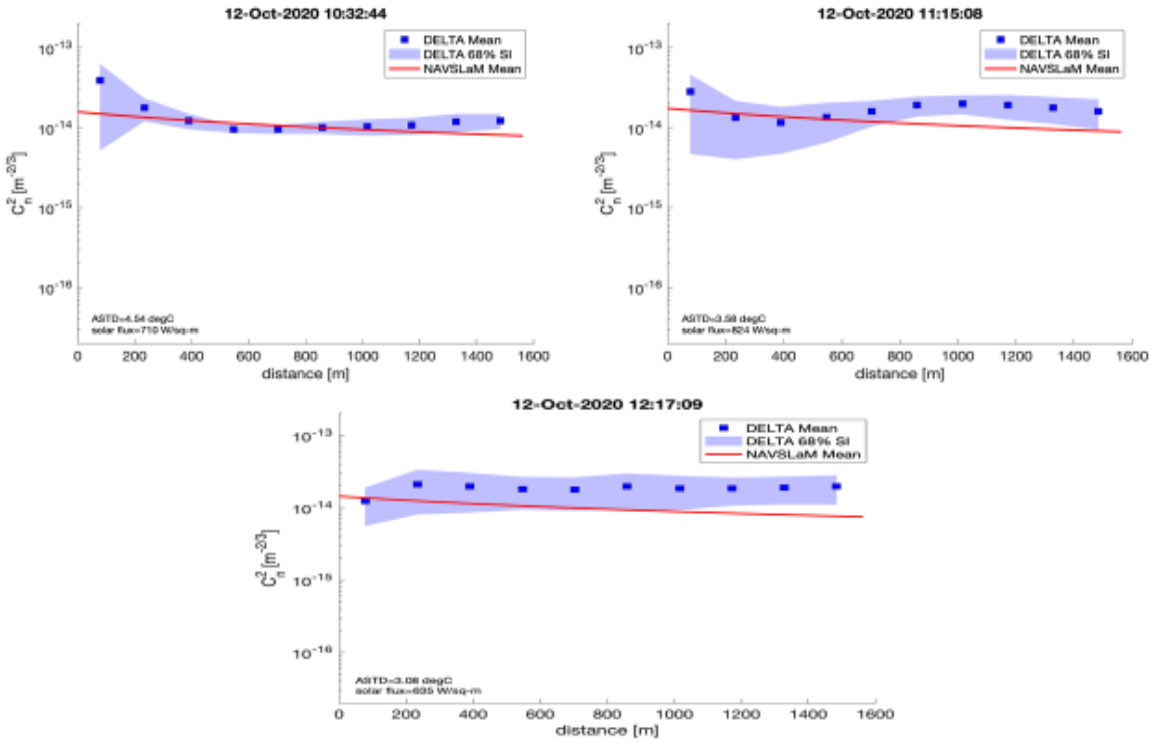

Figure 44. Comparative plots between DELTA and NAVSLaM provided profiles for 12 October 2020

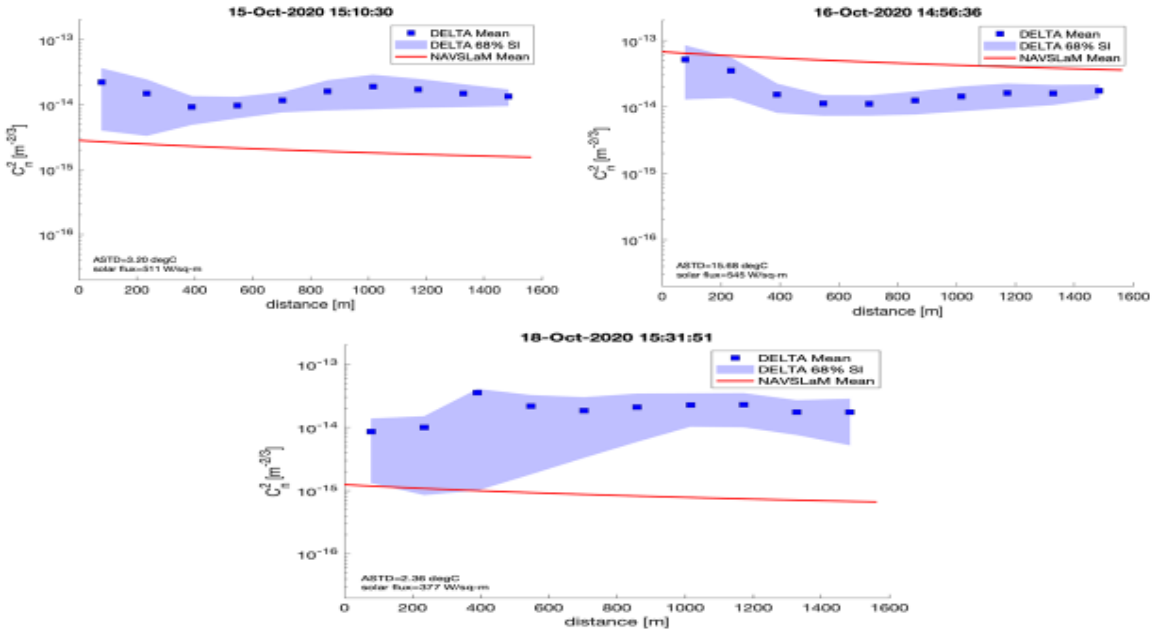

Figure 45. Comparative plots between DELTA and NAVSLaM provided profiles for 15,16 and 18 October 2020

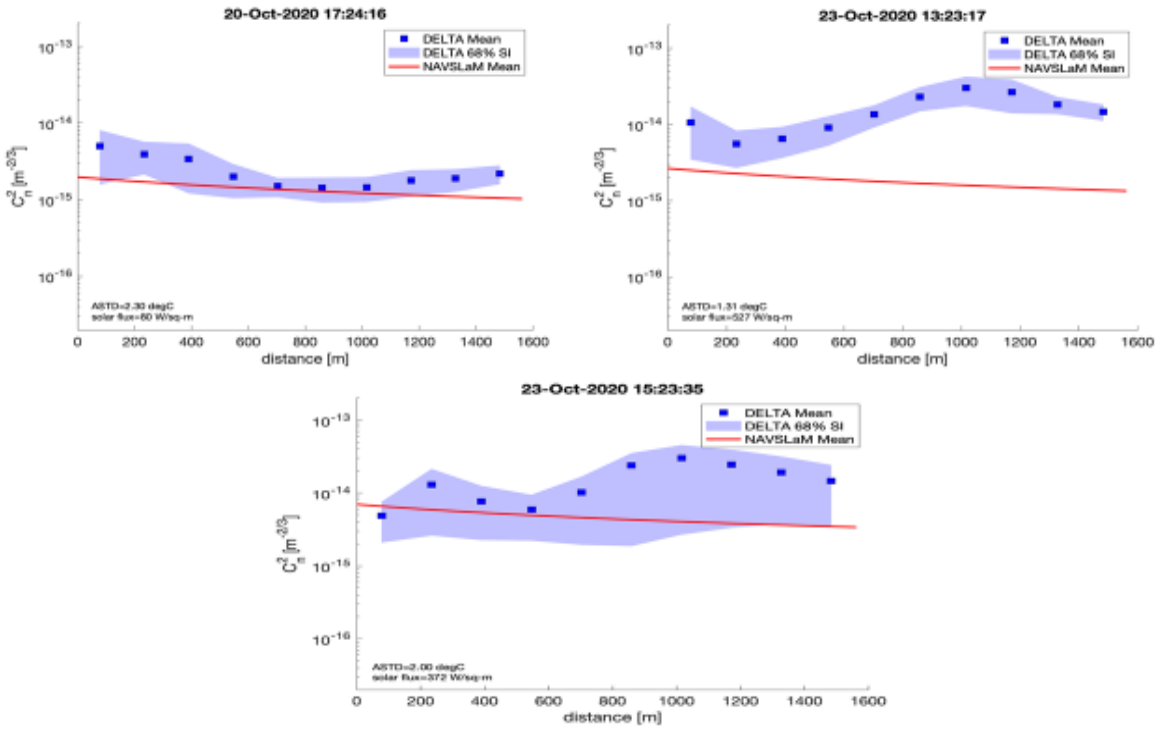

Figure 46. Comparative plots between DELTA and NAVSLaM provided profiles for 20 and October 2020

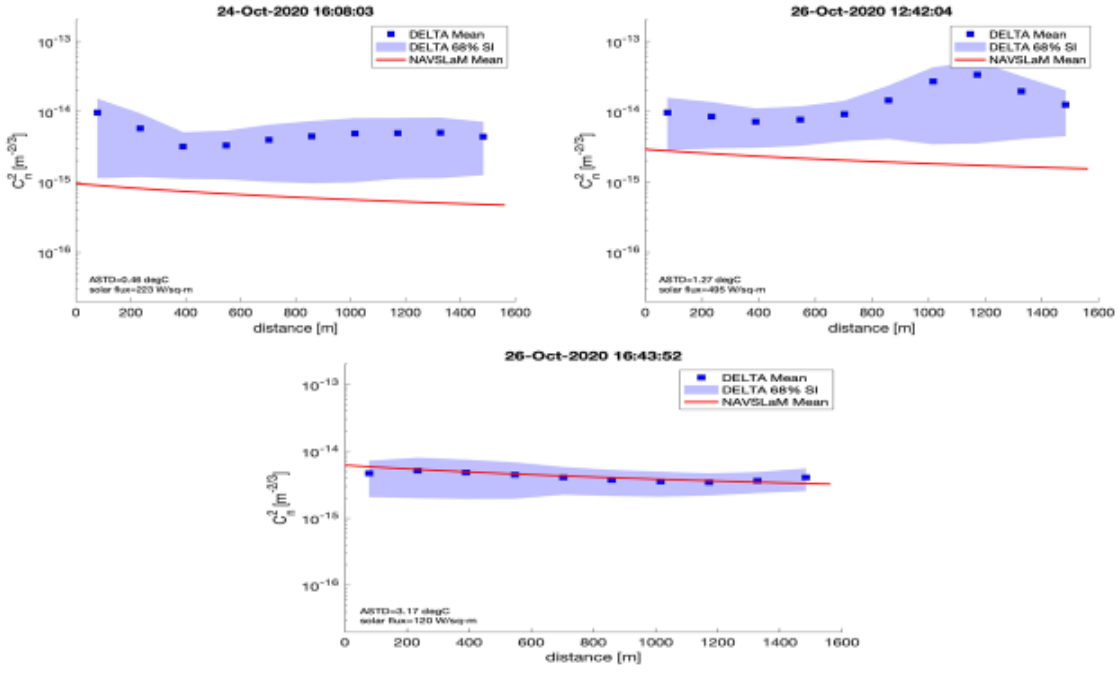

Figure 47. Comparative plots between DELTA and NAVSLaM provided profiles for 24 and 26 October 2020

B. REGRESSION MODEL BASED ON WEATHER STATION DATA

In addition to measuring turbulence directly, it is also desirable to determine if it is possible for turbulence to be predicted by a regression model based on the meteorological data obtained by the same weather stations mentioned in the previous section.

The collection of those meteorological parameters occurred at the same time as the DELTA measurements for the purpose of both training the regression learner model and testing the validity of the trained model. In total, 6083 turbulence measurements were recorded by the DELTA sensor over a span of approximately 101 hours spread over a two-month period (from 4 September 2020 to 26 October 2020); weather data was simultaneously collected by the WS-2000 and NOAA station, as well. The experimental measurements were, of course, not taken continuously but at gradual intervals of about two to four hours per day, due to the following limitations:

- The DELTA sensor requirement of illumination, i.e., the sensor is functional only during daylight hours when the target is visible.
- Due to the non-availability of power resources from the CG Pier facility, power was supplied by battery packs that only lasted for a few hours at a time.
- The presence of fog between the DELTA sensor and the target that reduced the visibility along the optical path to a great degree.

A machine learning regression method used for developing the model; specifically, a boosted-aggregated (bag) ensemble of regression trees (MATLAB function `fitrensemble ()`) with the following numerical parameters:

- The number of learning cycles: 500.
- The minimum leaf size: 1

These optimal parameters were determined via iterative search.

The following three of the total seven meteorological parameters provided by the weather stations were used as inputs to train the regression model:

- Wind speed (in meters per second),
- Air-sea temperature difference (ASTD, in degrees Celsius)
- Solar radiation flux (in watts per square meter).

The first two was selected based upon the inputs of NAVSLaM, which is a physics-based turbulence model; the solar flux was used since optical turbulence is driven via heat conduction from the ground to the air above it. The results that the model trained on are the $\log_{10}$ of the mean C_n^2 values reported by the DELTA.

The C_n^2 turbulence profile developed by both the regression model and the DELTA sensor measurements over the whole experimental period is illustrated in Figure 48. Since the data was collected on different days, the values are plotted against record number instead of time. The first 75% of the DELTA measurements were used to train the model (and indicated by blue + symbols). The remainder 25% of the DELTA measurements (red +) were used to test the predictive performance of the model. The Root Mean Square Error (RMSE) statistics measure was used to evaluate the model fit.

Overall, it is noticed that the regression model (yellow line) fits the training data set very well. The remaining 25% of the total measurements shows a satisfying (though not perfect) fit with the model. This indicates that regression analysis using machine learning techniques represents an attractive option for predicting the optical turbulence from a few simple measurements from a typical weather station.

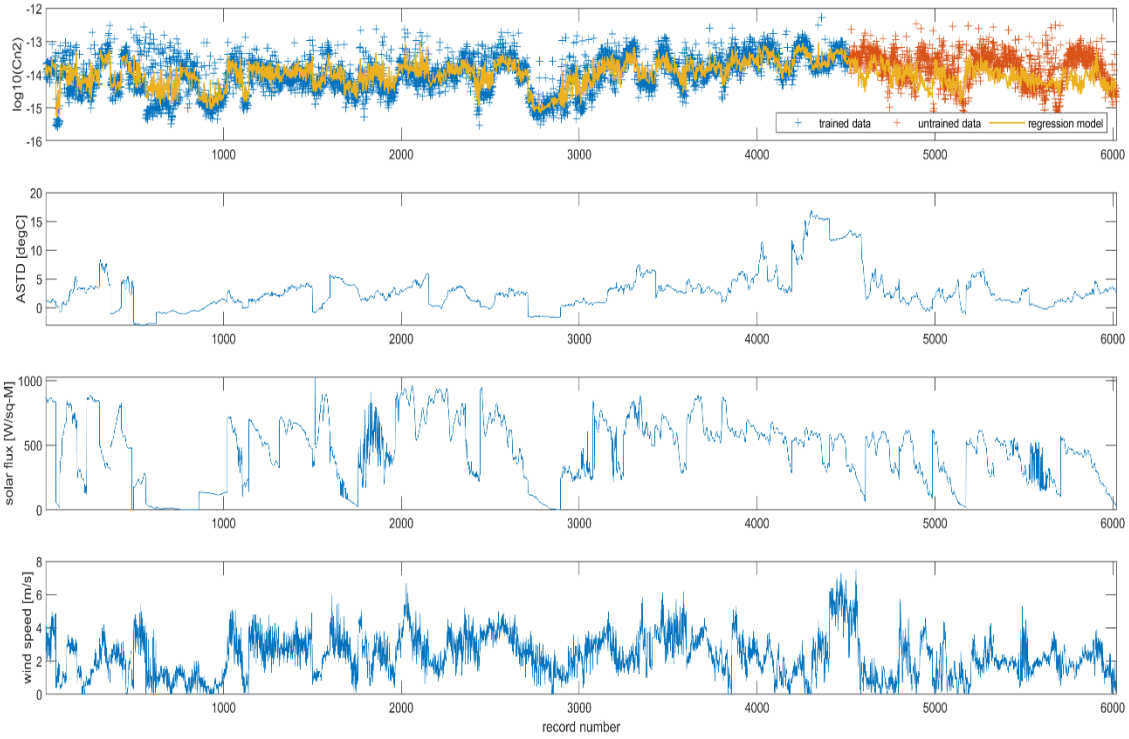

Figure 48. The C_n^2 turbulence profile provided by both the linear regression model and the DELTA sensor measurements (top), the ASTD (middle) , the solar flux (middle) and the wind speed (bottom) over the whole experimental period

Figure 49 the C_n^2 predicted by the regression model with both trained (blue +) and untrained (red +) data sets relative to the "true" values provided by the DELTA. Observing that figure, the following conclusions are drawn:

- The model fits the trained data set quite well as they follow the 45° slope line pretty closely, in contrast with the untrained data where the model seems to underestimate the true C_n^2 values in strong turbulence. Those data trends appear to be in agreement with the regression model C_n^2 profile shown on the top plot of Figure 48.

- The above-mentioned data trends with respect to the regression model are seen with the RMSE for the $log_{10}C_n^2$ values. Indeed, the $RMSE = 0.2260$ value for

the trained data are about half the corresponding value of $RMSE = 0.4485$ for untrained data. The larger RMSE value for the untrained data was expected, but it could be improved with more training data.

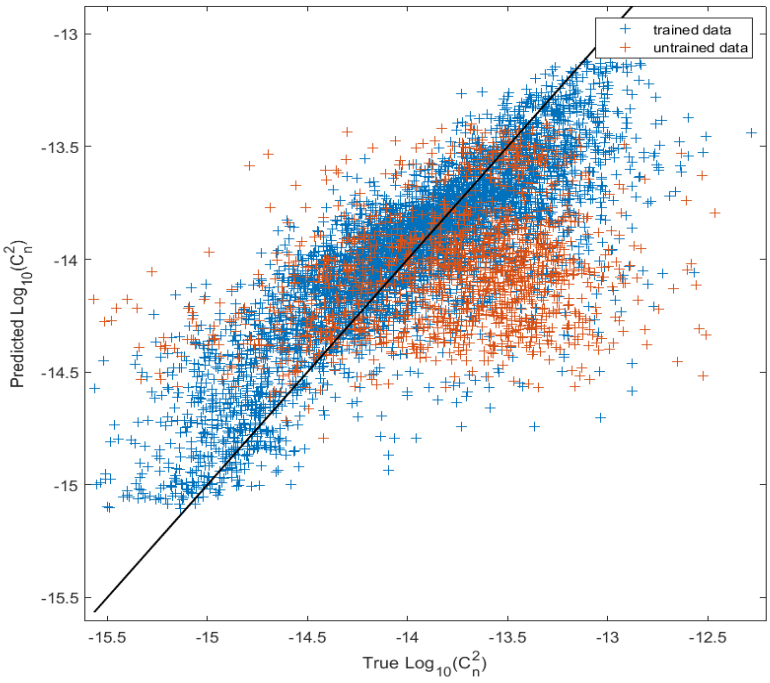

Figure 49. A quantitatively indicative plot of the regression model consistency rate with both trained and untrained data

Summarizing all of the above, it is concluded that although such a regression model is a very promising and simple approach for predicting the optical turbulence, its reliability is strongly related to the model validation by a large amount of the data collected over an extended time period and under various meteorological conditions.

C. IMPACT ON SNR OF AN FSO SYSTEM

At this section of the analysis chapter, a rough estimation of the impact that turbulence might have on the signal-to-noise ratio (SNR) of an FSO communication system is given. These results are based upon equation 27.

For the purposed of this study, the following parameters are used for a notional FSO link:

- The propagation length L=1563m
- The laser wavelength λ=1.5 μm
- The output power of the laser source $P_0 = 850$ mW
- The half-angle transmitter beam divergence θ=1 mrad
- The detector bandwidth B=1 GHz
- The detector temperature T=300 K
- The detector responsivity $R_{sp} = 0.5$ A/W
- The photodetector resistance R=50 Ω
- The attenuation of the system is not taken into account, i.e. ε=0.

The propagation distance was chosen to match the length of the DELTA path. Other parameters were chosen to represent typical values for an FSO system [16] to illustrate the effect that turbulence might have on a system.

Figure 50 illustrates the SNR of the laser communication system for different amounts of turbulence C_n^2 versus the diameter of the receiving aperture. From this figure, the following conclusions are drawn:

- In the idealized (i.e., no turbulence $C_n^2 = 0$) condition (blue line), the SNR increases for larger aperture diameters since more of the beacon light is intercepted and focused onto the detector.
- When non-zero turbulence conditions are applied, it is noticed a tremendous reduction of the SNR performance due to scintillation from turbulence. The yellow line represents the average C_n^2 measured by DELTA over the Monterey Bay (the average is carried out in log space). Clearly, the presence of turbulence

greatly reduces the SNR ratio. The SNR increases with larger apertures due to the increase in signal on the detector and from the aperture averaging effect discussed in Chapter III.

- The red and purple lines, which show a standard deviation from the mean C_n^2 towards weak and strong turbulence levels, respectively, seem to follow the same pattern as the yellow line does. The SNR ratio is still greatly affected by a relatively weak turbulence of $C_n^2 \approx 3 \times 10^{-15}\ \mathrm{m}^{-2/3}$.

- Other figures of merit regarding the performance of an FSO could be explored, including the probability of the bit detection and bit rate errors [15]. These areas will be left for future work.

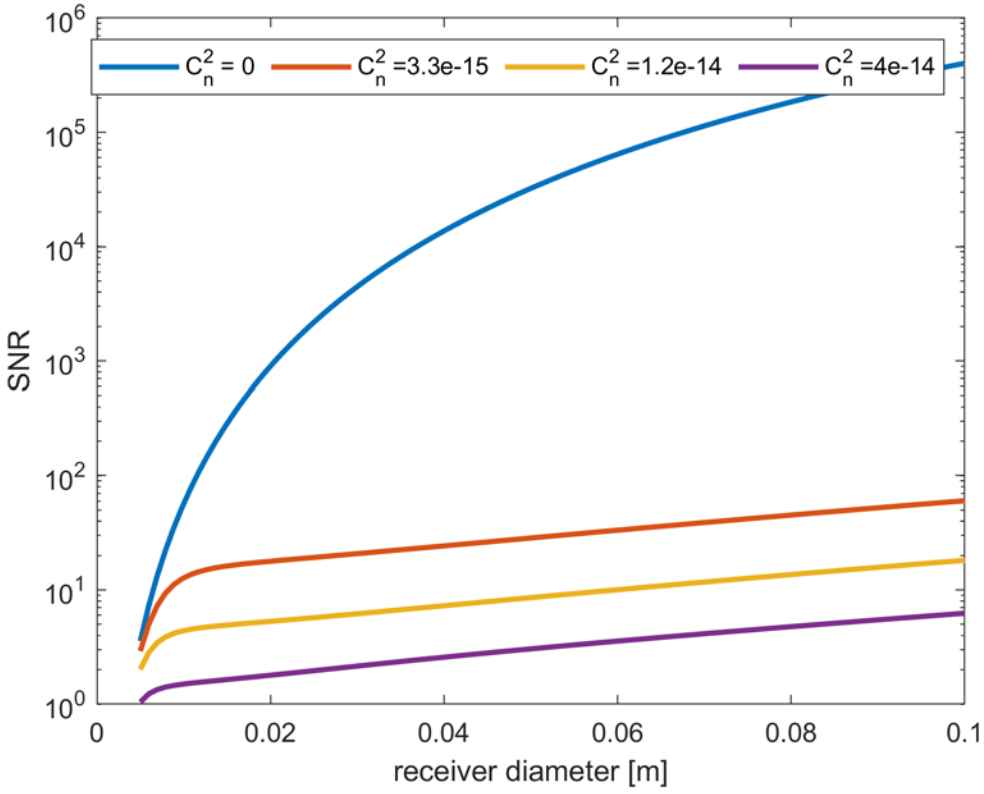

Figure 50. SNR performance of an FSO system under various turbulence conditions

VI. CONCLUSION AND FUTURE WORK

The main purpose of this thesis was to compare measurements and models of atmospheric turbulence in a maritime environment. Various experiments were done to estimate C_n^2 values over the Monterey Bay using measurements from various sensors such as the CSAT3 sonic anemometer and a fine wire thermocouple on board NOAA ships and the MZA DELTA on the Coast Guard pier. The resulting C_n^2 values were compared to predictions by NAVSLaM and a machine learning regression analysis model, using the meteorological data provided by local weather stations. Also, the impact of turbulence on the signal-to-noise ratio (SNR) for a notional FSO system was estimated, showing that even moderate amounts of turbulence can significantly reduce the SNR.

However, though the goal of this thesis work was largely obtained by the in-depth study of optical turbulence behavior in a realistic maritime environment, there is always room for further improvement. Further analysis should be done to determine which sensors are most useful for estimating turbulence in the maritime environment. Also, in order to validate and improve the turbulence models, much more experimental measurements should be taken over an extended period of time under various weather conditions.

THIS PAGE INTENTIONALLY LEFT BLANK

LIST OF REFERENCES

[1] "Free-space optical communication," *Wikipedia.* Accessed March 2020. [Online]. Available: https://en.wikipedia.org/wiki/Free-space_optical_communication.

[2] Z. Ghassemlooy and W. O. Popoola, "Terrestrial free-space optical communications," in *Mobile and Wireless Communications: Network Layer and Circuit Level Design*, S. A. Fares and F. Adachi, Eds. London, England, UK: IntechOpen Limited, 2010. [Online]. pp. 355–392.

[3] "Atmospheric propagation," class notes for Electric Ship Weapon Systems, Phy. Dept., Naval Postgraduate School, Monterey, CA, USA, fall, 2020.

[4] A. K. Majumdar, "*Free-space laser communication performance in the atmospheric channel*," *J. Opt. Fiber Comm.* vol. 2, no. 2, pp. 345–396, Nov. 2005. [Online]. doi:10.1007/s10297-005-0054-0

[5] K. N. Liou, *An Introduction to Atmospheric Radiation*, 2nd ed. San Diego, CA, USA: Academic Press, 2002.

[6] "Mie scattering," *Wikipedia.* Accessed March 2020. [Online]. Available: https://en.wikipedia.org/wiki/Mie_scattering

[7] "Modeling optical turbulence and its impacts on HEL performance in a maritime environment," class notes for Electric Ship Weapon Systems, Phys. Dept., Naval Postgraduate School, Monterey, CA, USA, Fall, 2020.

[8] J. D. Schmidt, *Numerical Simulation of Optical Wave Propagation with Examples in MATLAB*, Bellingham, WA, USA: Society of Photo-Optical Instrumentation Engineers (SPIE), 2010.

[9] A. K. Majumdar and J. C. Ricklin, *Free-space Laser Communications, Principles and Advances*, New York, NY, USA: Springer Science and Business Media, 2008.

[10] G. P. Perram, S. J. Cusumano, R. L. Hengehold, and S. T. Fiorino, *Introduction to Laser Weapon Systems*, 1st ed. Albuquerque, NM, USA: Directed Energy Professional Society.2009.

[11] G. M. Anderson, *Development of a Standard Maritime C_n^2 Profile Using Satellite Measurements*. Wright-Patterson Air Force Base, OH, USA: Air Force Institute of Technology, March 2015.

[12] Ambient Weather WS-2000 WiFi OSPREY Solar-Powered Wireless Weather Station User's Manual, Version 1.4, Ambient LLC, 2018.

[13] CSAT3 Three Dimensional Sonic Anemometer Instruction Manual, Logan, UT, USA: Campbell Scientific, 1998.

[14] MZA DELTA Imaging Path Atmospheric Turbulence Monitor PM-02-600 User's Manual, Dayton, OH, USA: MZA Associates Corporation, 2018.

[15] Heba Yuksel, *Studies of the effects of atmospheric turbulence on free space optical communications*, Ph.d dissertation, Dept. of Electrical and Computer Enginnering, University of Maryland, College Park, MD, USA, 2005.

[16] A. Lionis, K. Peppas, H.E. Nistazakis, A.D. Tsigopoulos and K. Cohn, *Experimental perfomance analysis of a laser communication channel over maritime environment,*2020 [Online].Available: https://www.mdpi.com/2079-9292/9/7/1109

INITIAL DISTRIBUTION LIST

1. Defense Technical Information Center
   Ft. Belvoir, Virginia

2. Dudley Knox Library
   Naval Postgraduate School
   Monterey, California